

# Dispersion of solids in fracturing flows of yield stress fluids

S. Hormozi<sup>1,†</sup> and I. A. Frigaard<sup>2</sup>

<sup>1</sup>Department of Mechanical Engineering, Ohio University, 251 Stocker Center, Athens, OH 45701, USA

<sup>2</sup>Departments of Mathematics and Mechanical Engineering, University of British Columbia,  
1984 Mathematics Road, Vancouver, BC, Canada V6T 1Z2

(Received 27 July 2016; revised 1 May 2017; accepted 3 July 2017;  
first published online 29 September 2017)

Solids dispersion is an important part of hydraulic fracturing, both in helping to understand phenomena such as tip screen-out and spreading of the pad, and in new process variations such as cyclic pumping of proppant. Whereas many frac fluids have low viscosity, e.g. slickwater, others transport proppant through increased viscosity. In this context, one method for influencing both dispersion and solids-carrying capacity is to use a yield stress fluid as the frac fluid. We propose a model framework for this scenario and analyse one of the simplifications. A key effect of including a yield stress is to focus high shear rates near the fracture walls. In typical fracturing flows this results in a large variation in shear rates across the fracture. In using shear-thinning viscous frac fluids, flows may vary significantly on the particle scale, from Stokesian behaviour to inertial behaviour across the width of the fracture. Equally, according to the flow rates, Hele-Shaw style models give way at higher Reynolds number to those in which inertia must be considered. We develop a model framework able to include this range of flows, while still representing a significant simplification over fully three-dimensional computations. In relatively straight fractures and for fluids of moderate rheology, this simplifies into a one-dimensional model that predicts the solids concentration along a streamline within the fracture. We use this model to make estimates of the streamwise dispersion in various relevant scenarios. This model framework also predicts the transverse distributions of the solid volume fraction and velocity profiles as well as their evolutions along the flow part.

**Key words:** Hele-Shaw flows, plastic materials, suspensions

---

## 1. Introduction

In hydraulic fracturing, specially engineered suspensions are pumped at high pressure and rate into the reservoir, causing a propagating fracture to open. When the pressure is released the fracture is held open by packed grains of solid proppant (typically natural angular sand) that are left behind. This method increases the hydraulic conductivity and consequently enhances well production. At various stages in the process, streamwise dispersion of proppant can be important, e.g. tip screen-out

† Email address for correspondence: [hormozi@ohio.edu](mailto:hormozi@ohio.edu)

and spreading of the pad. Streamwise dispersion is also critically important in a recent process variation called the channel fracturing technique (CFT) (Gillard *et al.* 2010). The key concept here is to substitute the usual continuous stream of proppant slurry that fills the fracture with discrete pillars of proppant that hold open the fracture. The increased hydraulic conductivity of the clear channels between the pillars has the overall effect of a significant increase in fracture conductivity. To produce the pillar configuration in the fracture, slugs of proppant are interspersed with clear fracturing fluid at the wellhead. Eventually it is expected that these slugs enter the fracture, and remain distinct for sufficiently long for the fracture to close on them. Proper design of this pumping technique obviously requires an understanding of dispersion mechanisms, both in the well and along the fracture. One proposed method for controlling dispersion is via the frac fluid rheology and in particular use of a yield stress fluid, which may also enhance the transport capacity. In this study we aim to develop a model framework for studying these flows within the fracture, with a particular emphasis on streamwise dispersion and shear-thinning yield stress frac fluids.

By design, our study cuts across many related areas. There are many examples of using the Hele-Shaw approach to model fracture flows (e.g. Pearson 1994; Hammond 1995; Mobbs & Hammond 2001; Lakhtychkin, Vinogradov and Eskin 2011; Boronin & Osiptsov 2014; Boronin, Osiptsov & Desroches 2015), wherein the assumption is made that the velocity field and gradients can be scaled differentially, according to the fracture aspect ratio. This allows the neglect of the inertial terms under the assumption that the bulk flow Reynolds number,  $Re$ , multiplied by a small width-to-length ratio, is vanishingly small. On the experimental front, there are also experimental studies in Hele-Shaw cell geometries on viscous fingering (e.g. Buka, Kertesz & Vicsek 1986; Buka & Palfy-Muhoray 1987; Lemaire *et al.* 1991; Lindner, Coussot & Bonn 2000; Lindner *et al.* 2002; Makino *et al.* 2002) and on fracturing flows (e.g. Lyon & Leal 1998; Liu, Gadde & Sharma 2007). In real fractures and under realistic process conditions, geometric and inertial effects may become significant and there is a significant literature on improving the Hele-Shaw approach. Low- $Re$  experiments and computations through laboratory-produced fractures or computer-generated fractures have shown that reasonable corrections can be made for roughness and tortuosity at zero  $Re$  (e.g. Patir & Cheng 1978; Brown 1987; Zimmerman, Kumar & Bodvarsson 1991). These studies typically correct the usual (Newtonian) cubic flow law via definition of an appropriate hydraulic gap width, proposing corrections that depend on dimensionless geometric ratios such as the standard deviation to mean gap width, wavelength to mean gap width, etc.

Some of these flow laws extend to non-zero  $Re$  (e.g. Hasegawa & Izuchi 1983). Apart from via simulation, it is often hard to decouple purely geometric effects from inertial effects in studying the flows through fractures. Thus, for example, Yeo, De Freitas & Zimmerman (1998) constructed artificial sandstone fractures and compared the results of flow tests with numerical simulations based on the Reynolds equation, reporting 20–25 % discrepancies for  $18 < Re < 60$ . Following the use of the hydraulic gap width from Hasegawa & Izuchi (1983), the error was reduced by around a third. However, it is notable that significant errors persist at smaller  $Re$  than might be considered from a strict scaling analysis. There are also classical inertial corrections such as the Forchheimer correction (used in porous media flows) and the Ergun equations (used in packed beds).

There have been long-standing attempts to model non-Newtonian effects in porous media – see e.g. the fine early review of Savins (1969) – but less specifically directed

at yield stress fluids. Typically the end result is a specification of a non-Darcy (or nonlinear filtration) closure law relating superficial velocity to pressure gradients. In the case of yield stress fluids, these are generally of limiting pressure gradient type (e.g. Sultanov 1960; Entov 1967). Included in these studies and of relevance to fracture flows are some detailed two-dimensional (2D) studies: along wavy walled channels (Balhoff & Thompson 2004; Frigaard & Ryan 2004; Putz, Frigaard & Martinez 2009; Roustaei & Frigaard 2013), through bed/fibre-type geometries (Bleyer & Coussot 2014; Shahsavari & McKinley 2016), or other geometric variants (Roustaei, Gosselin & Frigaard 2015; Roustaei *et al.* 2016). There is also some limited study of inertial effects Roustaei & Frigaard (2015). In summary, these studies show that the simplistic picture of a plane Poiseuille flow with a rigid central plug is quickly destroyed by streamwise geometric variation, that new non-Darcy effects emerge via static fouling of deep wall undulations or roughness, but that suitable flow laws and limiting pressure gradient closures can be derived for specific classes of geometry.

In considering flows of yield stress fluid suspensions, we need to consider additional complexities: the frac fluid is now strongly shear thinning and, apart from a generic rheological description, process conditions can have a significant impact on the local conditions felt by particles. These conditions and effects are analysed later in this paper (§ 2.2), but to pre-empt, we find that fracture flows of yield stress fluids are unusual in allowing for a massive variation in local strain rates and effective viscosity. The consequence is that for many typical fracture flows the particle dynamics ranges from Stokesian in the fracture centre to significantly inertial close to the fracture walls. The local rheological behaviour of yield stress fluid suspensions in the Stokesian regime has recently been characterized (at least approximately) by Ovarlez, Bertrand & Rodts (2006), Chateau, Ovarlez & Luu Trung (2008), Mahaut *et al.* (2008), Coussot *et al.* (2009), Vu, Ovarlez & Chateau (2010), Ovarlez *et al.* (2012), Dagois-Bohy *et al.* (2015) and Ovarlez *et al.* (2015). We utilize these results below.

In particulate flows, the particle distribution results from hydrodynamics and multi-body interactions of the particles. In a non-homogeneous shear flow of Newtonian suspensions, it is observed that particles migrate from high- to low-shear-rate regions (Leighton & Acrivos 1987; Phillips *et al.* 1992). This has been modelled phenomenologically by attributing shear-induced diffusive migration to a combination of collisional Brownian motion and viscosity variation effects. These components have measured experimentally for Newtonian suspensions by Gadala-Maria & Acrivos (1980), Chapman (1990), Phillips *et al.* (1992), Hampton *et al.* (1997), Lyon & Leal (1998) and Snook, Butler & Guazzelli (2016). A different approach is the suspension balance model (SBM), which is a hybrid theoretical–phenomenological approach in which particle migration is modelled through normal stress gradients in the particle phase. The various constants and multipliers in this approach are determined from experimental measurements and numerical simulations (e.g. Morris & Boulay 1999). Although there are still unanswered questions and ongoing debate on the nature of particle stress in Newtonian suspensions (e.g. Lhuillier 2009; Nott, Guazzelli & Pouliquen 2011; Guazzelli & Morris 2012; Brady 2015), numerous experimental and computational studies have been conducted that support and advance this approach (e.g. Chapman 1990; Phillips *et al.* 1992; Merhi *et al.* 2005; Morris 2009; Dbouk, Lobry & Lemaire 2013).

The above solids dispersion models are largely restricted to Stokesian regimes and Newtonian fluids. In the fracturing context, geometric, inertial and rheological complexities are present. Neglecting the particles, there is a growing literature on

dispersion in fractures (e.g. Drazer & Koplik 2000, 2002; Auradou *et al.* 2005, 2006). As with porous media dispersivities, there is considerable anisotropy due to the flow direction and fracture geometry. More recent studies have considered the effects of shear-thinning rheology on tracer dispersion Boschan *et al.* (2007), Auradou *et al.* (2008), Boschan *et al.* (2008, 2009). One of the main features of these studies and others that focus purely on fluid flow (e.g. Skjetne, Hansen & Gudmondson 1999) is that at moderate  $Re$  the flow tends to channel through a (smoothed) central part of the fracture, leaving significant parts of the fracture with near-zero velocity, whereas creeping flows tend to fill the fracture. Similar effects were found with yield stress fluids by Roustaei & Frigaard (2015) and Roustaei *et al.* (2015). These features can have a significant effect on dispersion. It appears that there is relatively little work concerned with suspensions directly in this context.

The main novel contributions of our study are as follows. Firstly, we carry out an order-of-magnitude analysis of proppant transport along typical hydraulic fractures using viscous fluids (shear thinning and yield stress), specifically focusing on the macroscale flow and the particle scale. We include recent rheological models for yield stress suspensions, in which the presence of particles increases local strain rates, thus reducing local effective viscosity. Through our analysis we show that typical suspensions in hydraulic fracturing flows exhibit a transition from Stokesian to inertial regimes, on the particle scale, as we move across the fracture width (§ 2.2). Secondly, we develop a two-phase continuum framework for modelling fracturing flows, based on the SBM of Nott & Brady (1994). Owing to the particle-scale behaviour and the nature of the fluids, we extend the SBM approach in two directions: (i) we incorporate the shear-thinning yield stress rheology of the fluid; (ii) we incorporate inertial/unsteady ranges of particle behaviour using an order-of-magnitude analysis of the different flow regimes. We also incorporate in our model closure expressions for the various forces experienced by the particles, but only so far as to give an estimate of the size of these effects (§ 2.4). Thirdly, we reduce the overall model using scaling arguments to arrive at two tractable systems of reduced equations that model these flows, depending on whether or not the macroscale effects of inertia are negligible, which depends on the usual lubrication modelling criterion of  $Re\delta_i \ll 1$  ( $Re$  being the Reynolds number and  $\delta_i$  a suitable aspect ratio). Both systems (see § 3) result in 2D models of the in-plane flow variables and distribution of proppant. Finally in § 4 we explore a simplification of the lubrication model ( $Re\delta_i \ll 1$ ) that allows a one-dimensional (1D) model of proppant dispersion along a streamline of the width-averaged flow. We find that to leading-order dispersion is advective not diffusive, and use this model to study pulsed proppant distributions such as in the CFT. In addition, we obtain the transverse distributions of the solid volume fraction and velocity profiles as well as their evolutions along the flow part.

## 2. Flow regimes in fractures

A difficulty in modelling many industrial processes is the wide range of operational regimes and parameters. From a fluid mechanics perspective, we need to understand the influence of operational parameters on the flows, defining what are typical flows and identifying the key characteristics. This is the goal here. We first discuss some general parameter ranges directly below. We then address the rheology of viscoplastic suspension flows under shear in § 2.1. Section 2.3 groups bulk fracture flows broadly into three types, each of which shows different characteristic variations in strain rate and local effective viscosity across the fracture. The consequences of this variation are

discussed in § 2.3, from the perspective of regimes that the particle experiences, and this is put in the context of recent dimensional scaling studies. In summary, we build a comprehensive physical intuition of these flows before developing our continuum modelling approach in § 2.4.

### 2.1. Rheology

For a broad picture of the full range of complex fluids used in hydraulic fracturing, we refer the reader to the recent review of Barbati *et al.* (2016). As mentioned in the introduction, we focus on viscous frac fluids as opposed to slickwater slurries, and we target dispersive phenomena in proppant transport. Thus, shear rheology is more important than viscoelasticity for these aspects, although viscoelasticity is ever present in frac fluids. A wide range of fluids are used, according to operation and company, often with proprietary formulation, e.g. typically aqueous polymer gels (guar, hydroxypropyl guar (HPG), etc.), either linear gels or cross-linked (e.g. with borate). These fluids are quite viscous and often strongly shear thinning. A common oilfield characterization is via a power-law model, with consistency  $\hat{\kappa}_0 \approx 0.01\text{--}5 \text{ Pa s}^n$  and power-law index  $n \approx 0.2\text{--}1$ . Some fluids may have a modest yield stress,  $\hat{\tau}_{Y0} \approx 0\text{--}15 \text{ Pa}$ . For a typical frac fluid based on guar, we might expect  $0.35 < n < 0.6$  and  $0.1 < \hat{\kappa}_0 < 1 \text{ (Pa s}^n)$ . One also sees frac fluids with shear-thinning exponents in the  $0.2\text{--}0.3$  range, often with larger  $\hat{\kappa}_0$ . Rheological parameters are not independently variable. At high shear rates the effective viscosity tends to plateau, e.g. we would not expect the effective viscosity of viscous frac fluids to fall significantly below  $0.01 \text{ Pa s}$ .

To incorporate the range of shear rheologies, we will assume that the effective viscosity of the pure frac fluid is modelled reasonably well as a Herschel–Bulkley fluid, with effective viscosity  $\hat{\eta}_{f,0}(\hat{\gamma})$ , possibly bounded below at high shear. Ovarlez and co-workers have recently developed a general framework for shear-thinning and yield stress fluid suspensions that has been validated at least partially (see Ovarlez *et al.* 2006, 2012, 2015; Chateau *et al.* 2008; Mahaut *et al.* 2008; Coussot *et al.* 2009; Vu *et al.* 2010; Dagois-Bohy *et al.* 2015). The bulk suspension viscosity  $\hat{\eta}$ , is decomposed as

$$\hat{\eta} = \hat{\eta}_f \eta_r(\phi), \quad (2.1)$$

where  $\hat{\eta}_f$  is referred to as the liquid-phase viscosity and  $\eta_r(\phi)$  is the dimensionless relative viscosity, modelled for example by the Krieger–Dougherty law

$$\eta_r(\phi) = \left[ 1 - \frac{\phi}{\phi_m} \right]^{-2.5\phi_m}, \quad (2.2)$$

or a close variant (see Maron & Pierce 1956; Dougherty 1959; Krieger 1972; Quemada 1982). Apart from conceptual simplicity, there exist generalizations of such laws to particles of different shapes, e.g. rods/fibres (see Wierenga & Philips 1998). Here  $\phi_m$  denotes the maximal packing fraction. The relative viscosity is further decomposed into  $\eta_r(\phi) = \eta_p(\phi) + 1$ , where  $\eta_p(\phi)$  is called the particle-phase viscosity, satisfying  $\eta_p(\phi) \sim \phi$  as  $\phi \rightarrow 0$  and  $\eta_p(\phi) \rightarrow \infty$  as  $\phi \rightarrow \phi_m$ . The combination  $\hat{\eta}_f \eta_p(\phi)$  usually appears as part of the solids-phase stress.

In the liquid phase the particles act to amplify effects of a bulk shear rate imposed on the suspension, i.e. since the particles themselves do not deform. This amplification can be crudely estimated as

$$\hat{\gamma}_{loc} = \left[ \frac{\eta_r(\phi)}{1 - \phi} \right]^{1/2} \hat{\gamma}, \quad (2.3)$$

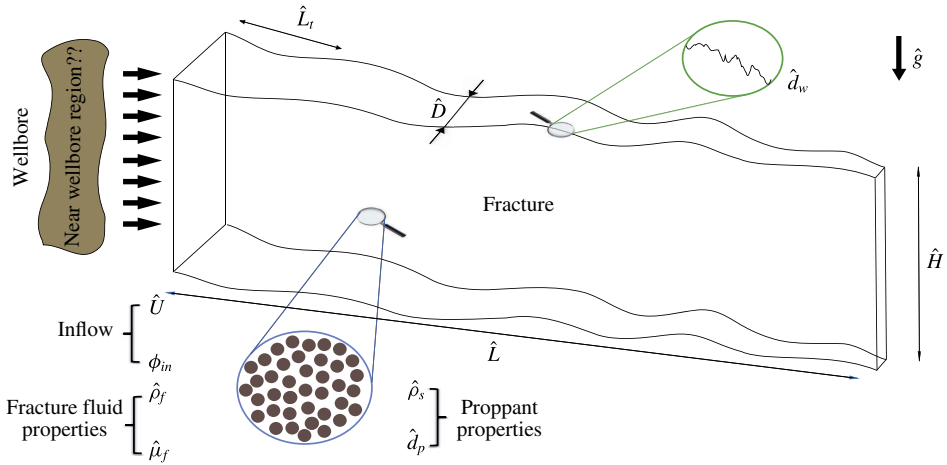


FIGURE 1. (Colour online) Schematic of a channel-like fracture. The solid phase, i.e. proppant with volume fraction  $\phi_{in}$ , is added at the inlet to the fracturing fluid in a cyclic fashion to produce a network of open channels.

which is verified reasonably well by experimental results (Ovarlez *et al.* 2006; Mahaut *et al.* 2008; Dagois-Bohy *et al.* 2015) and agrees with the theoretical considerations of Chateau *et al.* (2008). When the strain rate  $\hat{\gamma}$  is imposed on the suspension,  $\hat{\gamma}_{loc}$  is representative of that felt by the local fluid and particle, and assuming a Herschel–Bulkley type closure,

$$\hat{\eta}_f(\hat{\gamma}, \phi) = \hat{\eta}_{f,0}(\hat{\gamma}_{loc}(\phi)) = \hat{\kappa}_0 \left[ \frac{\eta_r(\phi)}{1 - \phi} \right]^{(n-1)/2} \hat{\gamma}^{n-1} + \frac{\hat{\tau}_{Y0}}{\hat{\gamma}} \left[ \frac{\eta_r(\phi)}{1 - \phi} \right]^{-1/2}. \quad (2.4)$$

This can be interpreted as assuming the liquid within the suspension obeys a Herschel–Bulkley type law, but with  $\phi$ -dependent consistency and yield stress defined by

$$\hat{\kappa} = \hat{\kappa}_0 \left[ \frac{\eta_r(\phi)}{1 - \phi} \right]^{(n-1)/2}, \quad \hat{\tau}_Y = \frac{\hat{\tau}_{Y0}}{\left[ \frac{\eta_r(\phi)}{1 - \phi} \right]^{1/2}}. \quad (2.5a,b)$$

When  $\eta_r(\phi)$  is included, the effective viscosity of the suspension increases with  $\phi$ , but note that the fluid viscosity ( $\hat{\eta}_f$  above) decreases with  $\phi$ .

### 2.2. Dimensional analysis

Figure 1 schematically illustrates a fracture, somewhat distant from the well. Fundamentally, this is a shear flow along a channel of varying width and orientation. We assume three characteristic lengths: width  $\hat{D}$  (5–25 mm), length  $\hat{L}$  (100–600 m) and height  $\hat{H}$  (20–100 m). We assume that in-plane variations occur on a length scale  $\hat{L}_t \lesssim \min\{\hat{L}, \hat{H}\}$ , where  $\hat{L}_t \gg \hat{D}$ . On a scale smaller than  $\hat{D}$ , one might also include a roughness scale  $\hat{d}_w$ .

The pumping process is modelled by a representative inflow velocity  $\hat{U}_0$  (0.1–3 m s<sup>-1</sup>), or alternatively a flow rate. Additionally we specify the inflowing

proppant solids fraction  $\phi_{in}$ , (typically 5%–40%). These variables will be time-varying in a complex pumping operation. As the slurry travels along the fracture, some of the frac fluid may leak off into the formation. This leads to higher solid volume fractions in the fracture. Although at times this is a significant effect, for now we focus only on transport along the fracture. Although a range of proppants may be used, common is a 20/40 mesh sand with approximately spherical particles, a representative diameter  $\hat{d}_p$  in the range 0.42–0.84 mm and density  $\hat{\rho}_s = 2650 \text{ kg m}^{-3}$ . Slurry rheology has been discussed in § 2.1. We assume a frac fluid density  $\hat{\rho}_f (\approx 1000 \text{ kg m}^{-3})$  and a representative viscosity  $\hat{\mu}_f$ .

Even with the simplistic description above, a minimum of 11 dimensional parameters arise, depending on three independent dimensions. Thus, we expect eight dimensionless groups (plus  $\phi_{in}$ ) to govern these flows. Five of these groups are geometric. The roughness  $\delta_w = \hat{d}_w / \hat{D} \ll 1$  we shall neglect for simplicity. On adopting  $\hat{D}$  and  $\hat{L}_t$  as natural length scales for transverse and streamwise directions, we have two groups,  $L = \hat{L} / \hat{D}$  and  $H = \hat{H} / \hat{D}$ , that simply indicate the extent of the fracture. More relevant to the transport processes are  $\delta_p = \hat{d}_p / \hat{D}$  and  $\delta_t = \hat{D} / \hat{L}_t$  i.e. a scaled particle diameter (ratio of particle diameter to fracture width) and the local fracture aspect ratio, respectively. Note that throughout this paper we write all dimensional quantities with a  $\hat{\cdot}$  symbol and dimensionless parameters without.

The remaining dimensionless groups include  $\phi_{in}$ , the density ratio  $s = \hat{\rho}_s / \hat{\rho}_f \approx 2.65$  and two others, namely the densimetric Froude number ( $Fr$ ) and Reynolds number ( $Re$ ):

$$Fr = \frac{\hat{U}_0}{\sqrt{\hat{g}(s-1)\hat{D}}}, \quad Re = \frac{\hat{\rho}_f \hat{U}_0 \hat{D}}{\hat{\mu}_f}. \tag{2.6a,b}$$

In characterizing the rheology, we would expect at least two dimensionless groups, e.g.  $n$  and a Bingham number  $B_l = \hat{\tau}_{Y0} / [\hat{k}_0(6\hat{U}_0/\hat{D})^n]$ . Here,  $\hat{\mu}_f$  is the effective viscosity of the suspending fluid and the Bingham number  $B_l$  is based on the nominal laminar wall shear rate,  $8\hat{U}_0/\hat{D}$ . Further dimensionless groups may arise in characterizing the suspension (e.g.  $\phi_m$ ) and in operational parameters.

### 2.3. Characteristics of fracture flows

In the above two subsections we have indicated the main ranges of slurry rheologies and other dimensional parameters that arise in hydraulic fracturing. In order to model these flows effectively, we need to consider the behaviour at both the bulk scale and the particle scale.

Regarding the bulk flow, pure liquid Reynolds numbers up to a maximum of  $(5-10) \times 10^3$  are possible, but would be reduced via the presence of particles. More typically  $Re \sim 10^2$  would be common in fracture transport regimes, reducing to zero in cases of screen-out. In considering asymptotic models of flow in long thin geometries, the leading-order inertial terms would be of size  $\delta_t Re$ . Thus, at the outset we deduce that, while non-inertial lubrication-type models have validity in suitably straight fractures, inertia of the bulk flow is important in more complex fractures even at moderate flow rates.

To understand the shear-rate regime with the fluids considered, note that a uniform channel flow of pure frac fluid ( $\phi = 0$ ) would have a layered structure consisting of an unyielded plug flow occupying a central fraction  $y_Y$  of the channel:

$$\frac{B_l}{y_Y} (1 - y_Y) \left( 1 - \frac{1}{n+1} y_Y - \frac{n}{n+1} y_Y^2 \right)^n = \left( \frac{3(2n+1)}{n} \right)^n \tag{2.7}$$

Flow type	Slow	Normal	Fast
Slurry mean velocity	Weak	Moderate	High
Viscosity/yield stress	High	Moderate	Low
$\phi$	Moderate–high	Moderate	Moderate–low
$\delta_r$	$\ll 1$	$\lesssim 10^{-2}$	$\lesssim 10^{-1}$
Pseudo-plug $y_Y$	40 %–85 %	15 %–40 %	0 %–15 %
Pseudo-plug viscosity (Pa s)	$\gtrsim 10$	$\gtrsim 1$	0.1–0.2
Pseudo-plug $St_p$	$\ll 1$	$\ll 1$	$\ll 1$
Wall layer viscosity (Pa s)	0.05–0.2	0.03–0.05	$\approx 0.01$
Wall layer $\hat{\gamma}_{loc}$ ( $s^{-1}$ )	$\lesssim 600$	300–1500	1000–3000
Wall layer $St_p$	$\lesssim 1$	1–10	1–20

TABLE 1. Fracture flow categories: slow, normal and fast. First four rows define the category in terms of operational parameter ranges (see § 2.2). Remaining rows characterize the flow structure.

( $y_Y \in [0, 1]$  is readily calculated numerically). Outside of the plug we have yielded shear layers approaching the wall. This simple model can be adapted here by adjusting  $B_l$  to include the effects of  $\phi$  and typical variations in rheology, to give some idea of the range of plug variation. We find that the plug could occupy between 10 % and 85 % of the width. Now we need to consider that the fracture is not uniform. For such fluids, slow geometric variations in the flow direction induce extensional stresses that break the plug. In such situations (e.g. Putz *et al.* 2009) we may assume the deviatoric stress remains just above the yield stress with the shear-rate scale determined by geometric variations, i.e. approximately  $\hat{\gamma} \gtrsim \hat{U}_0/\hat{L}_l$  here. Considering the various effects of extensional stresses, inertial stresses, irregular streamwise variations in geometry and potential transverse settling of dense particles, it is sensible to assume that any predicted plug region is effectively a low-shear pseudo-plug, rather than a rigid plug. Finally, let us note that this type of velocity profile (low-shear-rate pseudo-plug plus sheared wall layers) is found in various models for pressure-driven suspension flows, simply due to particle migration effects and regardless of non-Newtonian effects.

The structure of pseudo-plug and sheared wall layer is helpful in evaluating the local behaviour within the suspension, to which we now turn. First, given the relatively high shear rates and nature of the solids-phase, Brownian and colloidal interactions may be safely ignored. Key interactions are likely to be hydrodynamic and possibly collisional. Within the wide operational ranges of dimensional parameters outlined in § 2.2, we now consider combinations of parameters that produce characteristically different effects in the flow at both bulk and particle scales. For simplicity we categorize these as slow, normal and fast, as defined by the first four rows in table 1.

For each flow category we now use the rheological models outlined in § 2.1 together with (2.7) to estimate: (i) the width of the low-shear pseudo-plug; (ii) characteristic low-shear viscosities within the pseudo-plug; (iii) typical particle Stokes numbers within the pseudo-plug; (iv) minimal viscosities, found near the walls; (v) maximal local shear rates, found near the walls; and (vi) maximal particle Stokes numbers within the wall layers. These parameters are tabulated in the lower rows of table 1. This type of analysis is crude in not explicitly including particle migration effects, but does begin to paint a clearer picture of the flows encountered.



In general, the shear rate is relatively constant across the pseudo-plug and then increases continuously but sharply through the shear layers. Shear thinning together with the local strain-rate amplification of (2.3) result in significant centre-to-wall variations in local particle Stokes number ( $St_p$ ) given by

$$St_p = \frac{\hat{\rho}_s \hat{d}_p^2}{3\pi \hat{\eta}_f} \hat{\gamma}_{loc}, \quad (2.8)$$

which is interpreted as the ratio of the time scale for viscous drag to affect particle momentum and the characteristic time scale of the suspension:  $\sim 1/\hat{\gamma}_{loc}$ . Note that, since  $\delta_p \ll 1$ , transverse variations in both effective viscosity and shear rate (due to the bulk imposed flow) are felt and evaluated locally on the particle length scale.

The Stokes number gives a measure of fluid–solid coupling. As expected, considering the full range of likely process and geometric conditions, the pseudo-plug regions are completely non-inertial in all flow types:  $St_p \ll 1$ . The main differences are reflected in the size of the central low-shear region  $y_l$ . In moving from the pseudo-plug towards the wall,  $St_p$  increases due to both the increase in  $\hat{\gamma}_{loc}$  and the decrease in  $\hat{\eta}_f$ . For slow fracture flows we find  $St_p \lesssim 1$  throughout the fracture, whereas for normal flows  $St_p \geq 1$  for approximately half of the sheared layer, approaching  $\sim 10$  at the walls. For fast flows we would have  $1 \lesssim St_p \lesssim 20$  over approximately half the fracture width, for typical 20/40 proppant.

A representative particle Reynolds number is

$$Re_p = \frac{\hat{\rho}_f \hat{\gamma}_{loc} \hat{d}_p^2}{\hat{\eta}_f} = \frac{3\pi}{s} St_p, \quad (2.9)$$

which closely follows the variations in  $St_p$  across the fracture as  $3\pi/s \sim O(1)$ . While  $St_p$  and  $Re_p$  have similar size, the physical interpretation of these quantities is different. Larger  $Re_p \geq 1$  values imply that we enter a nonlinear regime of drag (viscous to inertial), whereas  $St_p \geq 1$  indicates that the particle velocity is not fully relaxed. The latter implies that the fluctuating components of the particle velocity becomes important. Commonly, this is represented via the granular or particle temperature  $\hat{\Theta} \geq 0$ , which is the root-mean-square fluctuating velocity of the particle phase. Temperature  $\hat{\Theta}$  is present throughout the flow, but in Stokesian regimes (such as within the pseudo-plug)  $\hat{\Theta}$  becomes very small, serving primarily to regularize diffusive fluxes (see e.g. Nott & Brady 1994). Particle temperature is more commonly used in kinetic theories of particle dynamics and in granular flows.

#### 2.4. Modelling flow in the fracture

The main modelling challenge is to allow for a broad range of both bulk-scale flow effects (arising from geometry and process variations) and particle-scale effects as we traverse the fracture width. We adopt a continuum approach in which variables are interpreted as being volume-averaged over a suitably chosen local averaging volume, but not time-averaged. (Note that for typical  $\delta_p \approx (2-4) \times 10^{-2}$ , we have 25–50 particle diameters across the fracture, so that we are close to the limit of validity of a continuum approach.) Operational choices, cyclical pumping (e.g. CFT), particle migration, the possibility of screen-out, etc. all combine to imply that models for transport along the fracture should consider a full range of  $\phi$ , from relatively dilute to concentrated suspensions.

The description emerging is of a Stokesian pseudo-plug layer bounded by shear layers in which inertial and unsteady fluid–particle coupling effects are progressively important towards the walls. Variables specific to solid or liquid phases are phase-averaged, defined using the characteristic function of the phase, the local instantaneous variable (e.g. solids-phase velocity) and a suitable smoothing or weighting function  $\mathcal{G}$  (see e.g. Drew 1983, []). Our dimensional variables will be denoted with a  $\hat{\cdot}$  throughout. The suspension mass and momentum balances are

$$\hat{\nabla} \cdot \hat{\mathbf{u}} = 0, \quad (2.10)$$

$$\frac{D}{D\hat{t}}[\hat{\rho}\hat{\mathbf{u}}] = \hat{\mathbf{b}} + \hat{\nabla} \cdot \hat{\boldsymbol{\Sigma}}, \quad (2.11)$$

where  $\hat{\mathbf{u}}$  is the volume-averaged suspension velocity,  $\hat{\mathbf{b}}$  and  $\hat{\boldsymbol{\Sigma}}$  are the volume-averaged suspension body force and stress tensor, respectively (see Batchelor 1970). The suspension stress  $\hat{\boldsymbol{\Sigma}}$  is often decomposed into individual contributions from both fluid and solid phases:

$$\hat{\boldsymbol{\Sigma}} = -\hat{p}_f \mathbf{I} + \hat{\boldsymbol{\tau}}_f + \hat{\boldsymbol{\Sigma}}_p. \quad (2.12)$$

The material derivative in (2.11) is

$$\frac{D}{D\hat{t}} = \frac{\partial}{\partial \hat{t}} + \hat{\mathbf{u}} \cdot \hat{\nabla}. \quad (2.13)$$

These equations are obtained by phase-averaging the individual equations for solid and liquid phases, then summing to eliminate the inter-phase terms. Thus, we also need to consider conservation equations for one phase, taken here as the solids phase:

$$\frac{\partial \phi}{\partial \hat{t}} + \hat{\nabla} \cdot [\phi \hat{\mathbf{u}}_p] = 0, \quad (2.14)$$

$$\hat{\rho}_s \frac{D_p}{D\hat{t}} \phi \hat{\mathbf{u}}_p = \hat{\nabla} \cdot \hat{\boldsymbol{\Sigma}}_p + \sum_{i=1}^{i=n_p} \int_{S_i} \mathbf{n} \cdot \hat{\boldsymbol{\sigma}} \mathcal{G} \, dS + \hat{\mathbf{b}}. \quad (2.15)$$

Here  $\hat{\mathbf{u}}_p$  is the phase-averaged particle velocity and  $\phi$  is the solids volume fraction. On the left-hand side of (2.15),  $D_p/D\hat{t}$  denotes the material derivative using  $\hat{\mathbf{u}}_p$  for the advective term. The first term on the right-hand side is the particle stress, i.e. particle contribution to the suspension stress. The second term is the volume-averaged traction on the particle surfaces and the last term is the average body force.

### 2.5. Developing the suspension balance framework

Diffusive and dispersive effects combine with the averaged forces acting on the solids phase to distribute the particles. The solid-phase mass conservation equation (2.14) is typically manipulated to give a transport equation for evolution of  $\phi$ . Note that the phase averaging adopted preserves the instantaneous dynamics of each configuration, so that (2.14) has no diffusive flux. At least two general approaches have been taken to model particle-phase diffusion: (i) the diffusive flux approach of Leighton & Acrivos (1987), modified by Phillips *et al.* (1992); and (ii) the SBM of Nott & Brady (1994).

Following the SBM approach here, the relative velocity ( $\hat{\mathbf{u}}_r = \hat{\mathbf{u}}_s - \hat{\mathbf{u}}_f$ ) is substituted into (2.14) to give

$$\begin{aligned} \frac{\partial \phi}{\partial \hat{t}} + \hat{\nabla} \cdot [\phi \hat{\mathbf{u}}] &= -\hat{\nabla} \cdot [\phi(\hat{\mathbf{u}}_p - \hat{\mathbf{u}})] = -\hat{\nabla} \cdot [\phi(1 - \phi)\hat{\mathbf{u}}_r] \\ &= \hat{\nabla} \cdot [\phi(1 - \phi)\hat{M}(\hat{\eta}_f, \hat{d}_p, \phi)\hat{\mathbf{f}}_D], \end{aligned} \tag{2.16}$$

where  $\hat{M}$  denotes the particle mobility and  $\hat{\mathbf{f}}_D$  is the phase-averaged particle drag force. The usual approach now is to consider (2.15) in the limit of small inertia, whereby  $\hat{\mathbf{f}}_D$  may be substituted into (2.16), leading to the divergence of the remaining terms on the right-hand side of (2.15).

More recently Lhuillier (2009) and Nott *et al.* (2011) have shown that the volume-averaged traction (second term on the right-hand side of (2.15)) may be expressed as the sum of a particle-averaged force and the negative divergence of the particle stress. In this sense, the particle stress does not contribute to the particle momentum equation. The only terms remaining on the right-hand side of (2.15) are the external body force and the particle-averaged force, which consists of the hydrodynamic forces, contact traction forces and interparticle forces. This questions the foundation of the SBM model in attributing the shear-induced particle migration to the divergence of particle-phase stress. However, Nott *et al.* (2011) showed that the particle-averaged force can itself be expressed in terms of an interphase drag force and the divergence of a stress tensor, which includes the effects of hydrodynamic, contact and interparticle forces. Consequently, the form of particle-phase momentum equation used in the SBM approach is correct, but using conventional closures for the interphase drag force and the stress tensor is currently under debate (see Lhuillier 2009; Nott *et al.* 2011; Brady 2015). Thus, we continue below to follow the classical SBM approach in developing our model, but incorporate the local viscosity of the shear-thinning yield stress suspension as outlined in §2.1, and other necessary extensions.

One advantage of the SBM approach is that the particle temperature is included, which is helpful for modelling non-Stokesian particle effects present in fracture flows, as we do below, and in interpreting the results. We therefore replace (2.15) with the solid momentum equation:

$$\hat{\rho}_s \phi \frac{D_p}{D\hat{t}} \hat{\mathbf{u}}_p = \hat{\mathbf{f}}_B + \hat{\mathbf{f}}_p + \hat{\nabla} \cdot \hat{\Sigma}_p. \tag{2.17}$$

The phase-averaged forces acting on the particles contribute to two terms:  $\hat{\mathbf{f}}_B$  representing the net solids-phase body force and  $\hat{\mathbf{f}}_p$  representing the hydrodynamic forces. The phase-averaged net solids-phase body force is

$$\hat{\mathbf{f}}_B = \phi[\hat{\rho}_s - \hat{\rho}_f]\mathbf{g}. \tag{2.18}$$

In this paper we simplify by assuming that the phase-averaged net particle force is given primarily by the drag force,  $\hat{\mathbf{f}}_p \approx \hat{\mathbf{f}}_D$ , neglecting all other hydrodynamic particle forces. This in turn is modelled via a hindered settling closure:

$$\hat{\mathbf{f}}_D = -\frac{3\phi\hat{\rho}_f C_D(Re_{p,i})}{4h(\phi)\hat{d}_p} |\hat{\mathbf{u}}_r| \hat{\mathbf{u}}_r. \tag{2.19}$$

We adopt the same framework as Ovarlez and co-workers. In Ovarlez *et al.* (2012) the authors study particle settling in yield stress fluids, perpendicular to the main direction of shear. They advocate using a Newtonian hindering function  $h(\phi)$ ,

$$h(\phi) = \frac{1 - \phi}{\eta_r(\phi)}, \tag{2.20}$$

to modify the single-particle settling speed. They identify two limits (a plastic regime and a viscous regime) in each of which they use a drag law incorporating  $\hat{\eta}_f(\hat{\gamma}, \phi)$ , as defined in (2.4). A quite similar usage of  $\hat{\eta}_f$  for fitting a drag coefficient is described in Tabuteau, Coussot & de Bruyn (2007). The drag coefficient  $C_D(Re_{p,l})$  is extended to cover inertial regimes, for which there are a number of similar closure laws. There is an advantage to having a drag coefficient closure law that is easily invertible, and consequently we adopt

$$C_D(Re_{p,l}) = \begin{cases} \frac{24}{Re_{p,l}}, & Re_{p,l} < 1.4, \\ \frac{A_{CD}}{Re_{p,l}^{0.625}}, & 1.4 \leq Re_{p,l} \leq 500, \end{cases} \tag{2.21}$$

where  $A_{CD} = 24/1.4^{0.375}$ . Note that the range of  $Re_{p,l} > 500$  is unlikely to be attained. The Reynolds number is based on  $\hat{\eta}_f(\hat{\gamma}, \phi)$  and  $|\hat{\mathbf{u}}_r|$ , i.e.

$$Re_{p,l} = \frac{\hat{\rho}_f |\hat{\mathbf{u}}_r| \hat{d}_p}{\hat{\eta}_f}. \tag{2.22}$$

Inverting (2.19), with the drag coefficient (2.21), leads straightforwardly to the relation  $\hat{\mathbf{u}}_r = -\hat{M}(\phi, \hat{\gamma}, |\hat{\mathbf{f}}_D|)\hat{\mathbf{f}}_D$ , required for (2.16). We specify a dimensionless version of the mobility  $\hat{M}$  later.

Returning to the SBM derivation, it is assumed that the left-hand side of (2.17) is relatively small (which would hold, for example, in conditions where the flow is steady, rectilinear and fully developed). In this case, we may write

$$\hat{\mathbf{f}}_D \approx -[\hat{\mathbf{f}}_B + \hat{\nabla} \cdot \hat{\Sigma}_p], \tag{2.23}$$

and the solids mass conservation equation becomes

$$\frac{\partial \phi}{\partial t} + \hat{\nabla} \cdot [\phi \hat{\mathbf{u}}] = -\hat{\nabla} \cdot [\phi(1 - \phi)\hat{M}(\phi, \hat{\gamma}, |\hat{\mathbf{f}}_D|)(\hat{\mathbf{f}}_B + \hat{\nabla} \cdot \hat{\Sigma}_p)]. \tag{2.24}$$

The particle stress tensor is usually modelled by the expression

$$\hat{\Sigma}_p = -\hat{\Pi} \mathbf{Z} + \hat{\eta}_f \eta_p(\phi) \hat{\gamma} \tag{2.25}$$

(see e.g. Fang *et al.* 2002). The second term in (2.25) is the particle shear stress term. The bulk rate-of-strain tensor for the suspension is  $\hat{\gamma} = \hat{\gamma}_{ij}$ . Note that the bulk suspension strain rate is

$$\hat{\gamma} = \left[ \frac{1}{2} \sum_{i,j=1}^3 \hat{\gamma}_{ij}^2 \right]^{1/2}. \tag{2.26}$$

The first term in (2.25) is a product of the particle pressure  $\hat{\Pi}$  and the tensor  $\mathbf{Z}$ , through which we account for normal stress differences. It is argued that a reasonable approximation to the tensor  $\mathbf{Z}$  is

$$\mathbf{Z} = \begin{pmatrix} \lambda_1 & 0 & 0 \\ 0 & \lambda_2 & 0 \\ 0 & 0 & \lambda_3 \end{pmatrix}, \tag{2.27}$$

where the directions  $x_1$  and  $x_2$  are in the plane of shear (here this would be locally aligned with the mean flow along the fracture). According to the scaling,  $\lambda_1 + \lambda_2 + \lambda_3 = 3$ , and from Brady & Morris (1997), a common choice for shear flow is  $\lambda_1 = \lambda_2 = 2\lambda_3 = 6/5$ . Other choices can be made if there is specific knowledge of the normal stress differences. The particle pressure is modelled using the particle temperature in place of the strain rate, considering that  $\hat{\gamma}^2 \propto \hat{d}_p^{-2} \hat{\Theta}$  in a homogeneous suspension. The form selected is

$$\hat{\Pi} = \hat{\eta}_f \hat{d}_p^{-1} \hat{\Theta}^{1/2} p(\phi), \quad p(\phi) = 2\sqrt{3} k_\phi \phi^{1/2} (\eta_p)^A. \tag{2.28a,b}$$

An evolution equation for  $\hat{\Theta}$  is derived in Nott & Brady (1994) as a simplified form of the mechanical energy balance for the particle phase:

$$3\hat{\rho}_s \phi C(\phi) \frac{D_p \hat{\Theta}}{D\hat{t}} = \hat{\Sigma}_p, \quad \hat{\gamma} + 4\sqrt{3} \hat{\eta}_f \hat{d}_p^{-2} \beta(\phi) \hat{\Theta}^{1/2} |\hat{\mathbf{u}}_r| - 12 \hat{\eta}_f \hat{d}_p^{-2} \alpha(\phi) \hat{\Theta} - \hat{\mathbf{V}} \cdot \hat{\mathbf{q}}. \tag{2.29}$$

There are slight differences due to our preference to work with the particle diameter rather than radius, and a factor of 1/3 absent in Nott & Brady (1994), compared to the usual definition of particle temperature. The heat-capacity term  $C(\phi)$  is not specified, and not used below. The functions  $\alpha(\phi)$  and  $\beta(\phi)$  are specified semi-empirically by considering different limits of the model. The field  $\hat{\mathbf{q}}$  represents the phase-averaged fluctuating component of the solids-phase dissipation, i.e.

$$\hat{\mathbf{q}} = -\langle \hat{\Sigma}'_p \cdot (\hat{\mathbf{u}}_p - \langle \hat{\mathbf{u}} \rangle_p) \rangle, \tag{2.30}$$

which is modelled via a Fourier-type ‘conductive heat flux’ law,

$$\hat{\mathbf{q}} = -3\hat{\eta}_f \kappa_\Theta(\phi) \hat{\mathbf{V}} \hat{\Theta}. \tag{2.31}$$

Although phenomenological in many respects the above model has proven successful in predicting solids-phase distributions in pressure-driven shear flows and many others.

### 2.6. Unsteady inertial effects

The model outlined above is the standard SBM approach, extended to include non-Newtonian frac fluids (§ 2.1) and steady inertial effects via the nonlinear drag regime. In fracturing flows, within the shear layers approaching the walls, unsteady inertial effects also arise. We now look in more detail at the response of the suspension in the different parts of the flow, with the aim of developing a rational framework that covers these effects.

Following Cassar, Nicolas & Pouliquen (2005) and Andreotti, Forterre & Pouliquen (2013) we consider a particle that accelerates within the suspension, under the

action of a pressure  $\hat{P}$  and drag force  $\hat{F}_d$ . The particle responds on at least three different microscopic time scales related to rearrangement of the suspension. Either  $\hat{P}$  is balanced by pure acceleration (leading to  $\hat{t}_1 \sim \hat{\rho}_s \hat{\Theta}^{1/2} \hat{d}_p / \hat{P}$ ), or  $\hat{P}$  is balanced by  $\hat{F}_d$ . The latter leads to  $\hat{t}_2$  ( $\sim \hat{\eta}_f / \hat{P}$ ) if the drag is principally viscous, or to  $\hat{t}_3$  ( $\sim \hat{d}_p \sqrt{\hat{\rho}_f C_D / \hat{P}}$ ) if the drag is principally inertial. When the suspension is itself under shear, there is also a macroscopic time scale arising from the strain rate. We have seen that the bulk strain rate ( $\hat{\gamma}$ ) is felt locally as  $\hat{\gamma}_{loc}$ , which is still macroscopic on the particle scale.

Comparison of the macroscopic time scale ( $\hat{\gamma}_{loc}^{-1}$ ), with each of  $\hat{t}_1$ – $\hat{t}_3$  leads to three dimensionless groups, the relative size of which determines the dominant characteristic behaviour of the suspension, i.e. at different positions across the fracture and in different types of bulk flow. For example, when  $\hat{t}_1 \gtrsim \hat{t}_2$  and  $\hat{t}_1 \gtrsim \hat{t}_3$ , the rate-limiting microscopic time scale is  $\hat{t}_1$  and suspension behaviour is described primarily by  $I = \hat{\gamma} \hat{t}_1$  (case I). In this regime particle inertia dominates. If  $\hat{t}_2 \gtrsim \hat{t}_1$  and  $\hat{t}_2 \gtrsim \hat{t}_3$ , then  $\hat{t}_2$  is the rate-limiting microscopic time scale and suspension behaviour is described primarily by  $J = \hat{\gamma} \hat{t}_2$  (case II: viscous drag regime). Finally, when  $\hat{t}_3$  is rate-limiting, we expect  $J_I = \hat{\gamma} \hat{t}_3$  to describe the suspension behaviour (case III: inertial drag regime).

These three microscopic regimes are plotted schematically in figure 2. Note that the drag coefficient  $C_D$  is used on the vertical axis in order to capture both viscous and inertial balances. The fluctuating component of velocity has characteristic size  $\hat{\Theta}^{1/2}$ , which is used to define a (fluctuating) particle Reynolds number:

$$Re_{p,\Theta} = \frac{\hat{\rho}_f \hat{d}_p \hat{\Theta}^{1/2}}{\hat{\eta}_f}. \quad (2.32)$$

Using  $Re_{p,\Theta}$  in the usual Stokesian drag law allows us to evaluate  $\hat{t}_1 / \hat{t}_2 = \sqrt{s Re_{p,\Theta} / 24} \propto \sqrt{St_{p,\Theta}}$ . One can similarly evaluate  $\hat{t}_1 / \hat{t}_3 \propto s^{1/2} Re_{p,\Theta}^{5/16}$ , over the inertial range likely in this process (and eventually  $\hat{t}_1 / \hat{t}_3 \propto s^{1/2}$  as  $Re_{p,\Theta} \rightarrow \infty$ ).

In each microscopic regime it is possible to derive order-of-magnitude estimates for the key terms in the solids-phase conservation laws, as was done by Jenkins & McTigue (1990) for the granular regime; see table 2. In table 2,  $\hat{h} = \hat{d}_p [\eta_r(\phi) / (1 - \phi)]^{-1/2}$  denotes a representative particle separation, estimated consistently with our earlier treatment of the local strain rate. Particle conductivity and dissipation terms are described later with the transport equation for  $\hat{\Theta}$  (see appendix A).

It remains to interpret the different fracture flows in terms of the localized suspension characteristics described above. To do this we balance  $\hat{\gamma}_{loc} \sim \hat{\Theta}^{1/2} / d_p$ , to enable us to relate  $St_{p,\Theta}$  to  $St_p$ . Note that  $\hat{\gamma}_{loc}$  is imposed by the macroscopic flow, whereas  $\hat{\Theta}^{1/2} / d_p$  is a measure of the local response of the fluctuating particle velocity to this strain rate. Figure 2 shows schematically where the (process-scale) fracture flows ‘live’ in terms of the  $(I, J, J_I)$  cartoon that indicates microscopic regimes. The arrows indicate the variation across the fracture from the pseudo-plug in the centre to more inertial and unsteady regimes at the fracture walls.

This schematic indicates to us how non-Stokesian effects enter as we move across the fracture width, and table 2 suggests the appropriate scaling for extending the different terms in the SBM. Although we take this approach below, it is not the only way to model and include inertial/unsteady effects in the SBM. An alternative

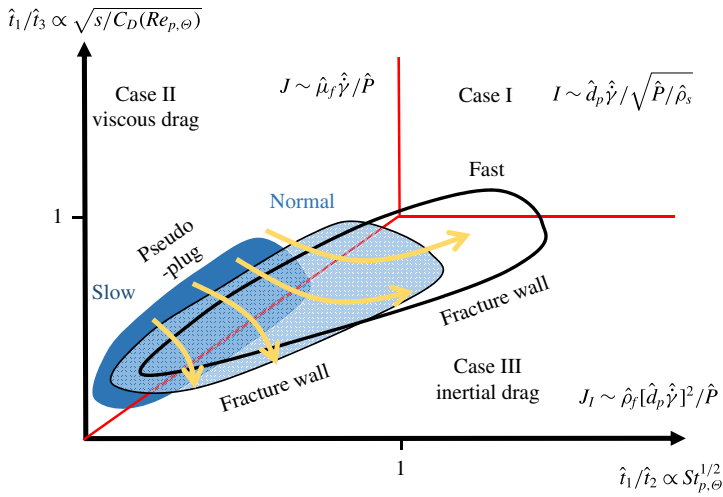


FIGURE 2. (Colour online) Variation of the local suspension regimes with slow, normal and fast fracture flows. The arrows indicate the variation across the fracture from the pseudo-plug in the centre to more inertial regimes at the fracture walls (styled after figure 7.13 in Andreotti *et al.* (2013)).

	Case I	Case II	Case III
Pressure	$\sim \frac{\hat{\rho}_s \hat{\Theta} \hat{d}_p}{\hat{h}}$	$\sim \frac{\hat{\eta}_f (1-e) \hat{\Theta}^{1/2}}{\hat{h}}$	$\sim \frac{\hat{\rho}_f \hat{\Theta} (1-e) \hat{d}_p}{\hat{h}}$
Viscosity	$\sim \frac{\hat{\rho}_s \hat{\Theta}^{1/2} \hat{d}_p^2}{\hat{h}}$	$\sim \frac{\hat{\eta}_f \hat{d}_p}{\hat{h}}$	$\sim \frac{\hat{\rho}_f \hat{\Theta}^{1/2} \hat{d}_p^2}{\hat{h}}$
Conductivity	$\sim \frac{\hat{\rho}_s \hat{\Theta}^{1/2} \hat{d}_p^2}{\hat{h}}$	$\sim \frac{\hat{\eta}_f \hat{d}_p}{\hat{h}}$	$\sim \frac{\hat{\rho}_f \hat{\Theta}^{1/2} \hat{d}_p^2}{\hat{h}}$
Dissipation	$\sim \frac{\hat{\rho}_s \hat{\Theta}^{3/2} (1-e)}{\hat{h}}$	$\sim \frac{\hat{\eta}_f \hat{\Theta}}{\hat{d}_p \hat{h}}$	$\sim \frac{\hat{\rho}_f \hat{\Theta}^{3/2} \hat{d}_p}{\hat{h}}$

TABLE 2. Scalings of solid-phase properties for cases I, II and III.

approach is to introduce an  $O(Re_{p,\Theta})$  ‘correction’ into the energy equation of the SBM (and into the other closures), drawing from kinetic theory. Closure models in these regimes have been developed by Koch and co-workers (e.g. Sangani *et al.* 1996; Wylie, Koch & Ladd 2003), targeted primarily at dense inertial gas suspensions, but also applicable to liquid suspensions with sufficiently large density ratio,  $s$ . An application of this style of model to slurry flows in fractures is developed by Eskin & Miller (2008). The gas kinetic theory closures are not strictly applicable for the  $s$  typical of fracturing flows, but this body of work does indicate the order of  $Re_{p,\Theta}$  correction. We outline this approach and compare with the direct scaling approach in appendix B.

In the Stokesian regime (case II) these scales are well known and those in table 2 are consistent with those of the SBM in Nott & Brady (1994). Comparing the scalings for case I with those for case II gives us the extension to the SBM closures

	Case I	Case II	Case III
Pressure	$\sim sRe_{p,\theta} \frac{\hat{\eta}_f \hat{\Theta}^{1/2}}{\hat{d}_p} p_0(\phi)$	$\frac{\hat{\eta}_f \hat{\Theta}^{1/2}}{\hat{d}_p} p_0(\phi)$	$\sim Re_{p,\theta} \frac{\hat{\eta}_f \hat{\Theta}^{1/2}}{\hat{d}_p} p_0(\phi)$
Viscosity	$\sim sRe_{p,\theta} \hat{\eta}_f \eta_p(\phi)$	$\hat{\eta}_f \eta_p(\phi)$	$\sim Re_{p,\theta} \hat{\eta}_f \eta_p(\phi)$
Conductivity	$\sim sRe_{p,\theta} \kappa_c \hat{\eta}_f \eta_p(\phi)$	$\kappa_c \hat{\eta}_f \eta_p(\phi)$	$\sim Re_{p,\theta} \kappa_c \hat{\eta}_f \eta_p(\phi)$
Dissipation	$\sim sRe_{p,\theta} \frac{\hat{\eta}_f \hat{\Theta}}{\hat{d}_p^2} \frac{\eta_p(\phi)}{\phi}$	$\frac{\hat{\eta}_f \hat{\Theta}}{\hat{d}_p^2} \frac{\eta_p(\phi)}{\phi}$	$\sim Re_{p,\theta} \frac{\hat{\eta}_f \hat{\Theta}}{\hat{d}_p^2} \frac{\eta_p(\phi)}{\phi}$

TABLE 3. Forms of solid-phase properties for cases I, II and III, scaled with the Stokesian case.

as we transition from Stokesian to the granular regime. Comparing the scalings for case III with those for case II gives us the extension to the SBM closures as we transition from Stokesian to the inertial hydrodynamic regime. The results of making these comparisons are illustrated in table 3. We observe that (dimensionally) the first column has a prefactor  $sRe_{p,\theta}$  compared to the Stokesian regime (case II), and the third column has a prefactor  $Re_{p,\theta}$ . The case III scalings are based on a fully inertial regime (in which the drag coefficient becomes Reynolds-invariant), but in this application we are still in the weakly inertial regime at the particle scale. Typically  $s \approx 2.65$  (sand–water), or sometimes  $s \approx 3-4$  (ceramic proppants), so that the relevant extensions to the Stokesian closures may be regarded as being of order  $Re_{p,\theta}$ .

Although we have used table 2 directly, the same order of magnitudes result on using the micro–macro time scale balances outlined above, which has some current popularity. A recent example of this is from Trulsson *et al.* (2012), who use a 2D computational approach to model the transition between case I and case II regimes. They show that the  $sRe_{p,\theta}$  prefactor is multiplied by a constant ( $\approx 0.6$  for the ranges studied). This suggests that the scaling approach followed here is valid and that we may also expect  $O(1)$  constant multipliers to the prefactors listed in table 3. Determination of these multipliers, however, requires extensive further experimentation and/or simulation, which is not our intent here. Instead, we assume constant unit multipliers for simplicity, which leads to the following extensions to the SBM closures:

$$\eta_s = \eta_p(\phi)(1 + sRe_{p,\theta}), \tag{2.33}$$

$$\Pi = \eta_f \Theta^{1/2} 2\sqrt{3} k_\phi \phi^{1/2} \eta_p(\phi)(1 + sRe_{p,\theta}), \tag{2.34}$$

$$\alpha = \frac{k_\alpha \eta_p(\phi)}{\phi} (1 + sRe_{p,\theta}), \tag{2.35}$$

$$\kappa_\theta = \kappa_c \eta_p(\phi)(1 + sRe_{p,\theta}). \tag{2.36}$$

### 3. Dimensionless model

To clarify the different physical effects present in the model derived in § 2.4, we scale the various equations. We assume a (locally) Cartesian coordinate system at any position along the fracture, with  $\hat{x}$  in the direction of flow,  $\hat{y}$  measured across the fracture and  $\hat{z}$  measured downwards, aligned with gravity. We define dimensionless



coordinates and velocity components as

$$(x, y, z) = \left( \frac{\hat{x}}{\hat{L}_t}, \frac{\hat{y}}{\hat{D}}, \frac{\hat{z}}{\hat{L}_t} \right), \quad (u, v, w) = \left( \frac{\hat{u}}{\hat{U}_0}, \delta_t \frac{\hat{v}}{\hat{U}_0}, \frac{\hat{w}}{\hat{U}_0} \right), \quad (3.1a,b)$$

and time is scaled with  $\hat{L}_t/\hat{U}_0$ . The scaled fracture has walls at  $y = -y_{w,-}(x, z)$  and  $y = y_{w,+}(x, z)$ . Recall that  $\delta_t = \hat{D}/\hat{L}_t \ll 1$  reflects the local aspect ratio of the fracture ( $\delta_t^{-1}$  is thus a representative distance along the fracture over which significant geometric changes take place). Components of the particle velocity and relative velocity are scaled in identical fashion. On applying this scaling, it follows that the leading-order strain rates are shear components in the plane of the fracture, of size  $\hat{U}_0/\hat{D}$ , with extensional strain rates  $O(\delta_t)$  smaller.

The extensional strain rates are felt primarily where the shear components vanish. As discussed in § 2.2, the slowly varying geometry tends to induce a pseudo-plug region in the fracture midplane within which the yield stress is marginally exceeded and the strain rates are of the size of the extensional strain rate. Although there are analyses of velocity profiles within such regions, these are geometry-specific and amount only to an  $O(\delta_t)$  correction. To include this geometric effect in a general (but phenomenological) way, we simply modify the strain rate as

$$\hat{\gamma} = \frac{\hat{U}_0}{\hat{D}} \dot{\gamma} = \frac{\hat{U}_0}{\hat{D}} \left[ \left( \frac{\partial u}{\partial y} \right)^2 + \left( \frac{\partial w}{\partial y} \right)^2 + \delta_t^2 \right]^{1/2}, \quad (3.2)$$

wherever it appears in the effective viscosity. This is essentially a regularization: the strain rate will not vanish in the pseudo-plug and the effective viscosity will remain finite. In the sheared layers (since  $\delta_t \ll 1$ ), this results in a minor perturbation to the leading-order shear stresses and flow.

As the leading-order strain rates are  $\sim \hat{U}_0/\hat{D}$ , we define a viscosity scale  $\hat{\eta}_0$  as

$$\hat{\eta}_0 = \hat{\kappa}_0 \left( \frac{\hat{U}_0}{\hat{D}} \right)^{n-1}, \quad (3.3)$$

which we use to scale all viscous terms. The dimensionless liquid-phase viscosity is

$$\eta_f(\dot{\gamma}, \phi) = [\dot{\gamma}_{loc}(\dot{\gamma}, \phi)]^{n-1} + \frac{B}{\dot{\gamma}_{loc}(\dot{\gamma}, \phi)}, \quad (3.4)$$

where  $\dot{\gamma}_{loc}(\dot{\gamma}, \phi)$  is a dimensionless local strain rate and  $B$  is the Bingham number:

$$\dot{\gamma}_{loc}(\dot{\gamma}, \phi) = \left[ \frac{\eta_r(\phi)}{1-\phi} \right]^{1/2} \dot{\gamma} = \left[ \frac{\eta_r(\phi)}{1-\phi} \right]^{1/2} \left[ \left( \frac{\partial u}{\partial y} \right)^2 + \left( \frac{\partial w}{\partial y} \right)^2 + \delta_t^2 \right]^{1/2}, \quad (3.5)$$

$$B = \frac{\hat{\tau}_{Y0} \hat{D}}{\hat{\eta}_0 \hat{U}_0} = \frac{\hat{\tau}_{Y0}}{\hat{\kappa}_0 \left( \frac{\hat{U}_0}{\hat{D}} \right)^n}. \quad (3.6)$$

The relative viscosity  $\eta_r(\phi)$  and particle-phase viscosity  $\eta_p(\phi)$  are already dimensionless.

To scale the remaining stresses, we need a scale for the particle temperature and the pressure. Considering the relation to the strain rate in a homogeneous sheared suspension, we write  $\hat{\Theta} = \delta_p^2 \hat{U}_0^2 \Theta$ . We scale the fluid pressure as

$$\hat{p}_f = \hat{\rho}_f \hat{g} \hat{z} + \frac{1}{\delta_t} \hat{\eta}_0 \frac{\hat{U}_0}{\hat{D}} p_f, \tag{3.7}$$

which anticipates the usual viscous shear-flow balance with the leading-order shear stresses. The hydrostatic component  $\hat{\rho}_f \hat{g} \hat{z}$  is subtracted from the total stress and included as part of the body force in the momentum equations. The remaining stresses, when scaled with  $\hat{\eta}_0 \hat{U}_0 / \hat{D}$  adopt the following form:

$$\Sigma = \underbrace{-\frac{1}{\delta_t} p_f \mathbf{I} + \eta_f \begin{pmatrix} O(\delta_t) & \frac{\partial u}{\partial y} & O(\delta_t) \\ \frac{\partial u}{\partial y} & O(\delta_t) & \frac{\partial w}{\partial y} \\ O(\delta_t) & \frac{\partial w}{\partial y} & O(\delta_t) \end{pmatrix}}_{\tau_f} - \underbrace{\eta_f \Theta^{1/2} p}_{\pi z} \begin{pmatrix} \lambda_1 & 0 & 0 \\ 0 & \lambda_2 & 0 \\ 0 & 0 & \lambda_3 \end{pmatrix} + \tau_p, \tag{3.8}$$

$$p = 2\sqrt{3} k_\phi \phi^{1/2} \eta_p(\phi) (1 + sRe_{p,\Theta}), \tag{3.9}$$

$$\tau_p = \eta_f \eta_p(\phi) (1 + sRe_{p,\Theta}) \begin{pmatrix} O(\delta_t) & \frac{\partial u}{\partial y} & O(\delta_t) \\ \frac{\partial u}{\partial y} & O(\delta_t) & \frac{\partial w}{\partial y} \\ O(\delta_t) & \frac{\partial w}{\partial y} & O(\delta_t) \end{pmatrix}. \tag{3.10}$$

Finally, we scale the phase-averaged particle forces with  $\hat{\eta}_0 \hat{U}_0 / \hat{d}_p^2$ . For the drag force we have

$$\mathbf{f}_D = - \begin{cases} \frac{18\phi\eta_f}{h(\phi)} \mathbf{u}_r, & \frac{\delta_p Re |\mathbf{u}_r|}{\eta_f} \leq 1.4, \\ \frac{18\phi\eta_f}{h(\phi)} \left( \frac{\delta_p Re |\mathbf{u}_r|}{1.4\eta_f} \right)^{3/8} \mathbf{u}_r, & \frac{\delta_p Re |\mathbf{u}_r|}{\eta_f} > 1.4, \end{cases} \tag{3.11}$$

where  $\mathbf{u}_r = (u_r, \delta_t v_r, w_r)$ . Alternatively, we can write the relative velocity in terms of a scaled mobility function,  $\mathbf{u}_r = -M(|\mathbf{f}_D|) \mathbf{f}_D$ :

$$\mathbf{u}_r = - \begin{cases} \frac{h(\phi)}{18\phi\eta_f} \mathbf{f}_D, & \frac{\delta_p Re h(\phi) |\mathbf{f}_D|}{18\phi\eta_f^2} \leq 1.4, \\ \frac{h(\phi)}{18\phi\eta_f} \left( 1.4 \frac{18\phi\eta_f^2}{\delta_p Re h(\phi) |\mathbf{f}_D|} \right)^{3/11} \mathbf{f}_D, & \frac{\delta_p Re h(\phi) |\mathbf{f}_D|}{18\phi\eta_f^2} > 1.4. \end{cases} \tag{3.12}$$

### 3.1. Scaled governing equations

The dimensionless suspension mass and momentum equations are:

$$0 = \nabla \cdot \mathbf{u} + \underbrace{O(\delta_t)}_{CT}, \tag{3.13}$$

$$\delta_t Re \frac{D}{Dt}(\rho u) = -\frac{\partial p_f}{\partial x} + \frac{\partial}{\partial y} \left[ \eta_f [1 + \eta_s] \frac{\partial u}{\partial y} \right] - \delta_t \lambda_x \frac{\partial \Pi}{\partial x} + \underbrace{O(\delta_t)}_{CT} + \underbrace{O(\delta_t^2)}_{SSG}, \quad (3.14)$$

$$\delta_t^3 Re \frac{D}{Dt}(\rho v) = -\frac{\partial p_f}{\partial y} - \delta_t \lambda_y \frac{\partial \Pi}{\partial y} + \underbrace{O(\delta_t^2)}_{CT} + \underbrace{O(\delta_t^2)}_{SSG}, \quad (3.15)$$

$$\delta_t Re \frac{D}{Dt}(\rho w) = \frac{Re}{Fr^2} \phi - \frac{\partial p_f}{\partial z} + \frac{\partial}{\partial y} \left[ \eta_f [1 + \eta_s] \frac{\partial w}{\partial y} \right] - \delta_t \lambda_z \frac{\partial \Pi}{\partial z} + \underbrace{O(\delta_t)}_{CT} + \underbrace{O(\delta_t^2)}_{SSG}. \quad (3.16)$$

The terms identified as *CT* and *SSG* indicate the next order of terms that enter the equations. Here *CT* denotes curvature terms, i.e. due to the streamwise variations in the local coordinate system. Similarly, *SSG* denote the next-order terms in the shear stress gradients.

We now consider the solids-phase momentum balance. The aim is to use the momentum balance to estimate the relative size of the drag force components and hence the relative velocity, which is needed in order to evaluate the solids-phase transport via the mass conservation equation, i.e. in (2.16). The *x*- and *z*-momentum equations are

$$\delta_t Re s \phi \frac{D_p}{Dt} u_p = \frac{f_{D,x} + f_{D',x}}{\delta_p^2} + \frac{\partial}{\partial y} \left[ \eta_f \eta_s \frac{\partial u}{\partial y} \right] - \delta_t \lambda_x \frac{\partial \Pi}{\partial x}, \quad (3.17)$$

$$\delta_t Re s \phi \frac{D_p}{Dt} w_p = \frac{Re}{Fr^2} \phi + \frac{f_{D,z} + f_{D',z}}{\delta_p^2} + \frac{\partial}{\partial y} \left[ \eta_f \eta_s \frac{\partial w}{\partial y} \right] - \delta_t \lambda_z \frac{\partial \Pi}{\partial z}, \quad (3.18)$$

where we have neglected terms of  $O(\delta_t)$  related to curvature and terms of  $O(\delta_t^2)$  related to shear stress gradients. The term  $f_{D'}$  denotes all forces other than drag and buoyancy that act on the particles. Assuming that  $\delta_t Re \lesssim O(1)$ , we see that the leading-order contributions to the drag force are

$$|f_{D,x}| \sim O(\delta_p^2) + |f_{D',x}|, \quad f_{D,z} \sim -f_{D',z} - \delta_p^2 \frac{Re}{Fr^2} \phi + O(\delta_p^2). \quad (3.19a,b)$$

Although we ignore  $f_{D'}$  in our reduced model later, we include here some discussion, as it is helpful for future modelling. Other than viscous drag and gravitational/buoyancy forces, a number of other forces act on particles immersed in a fluid (see e.g. Maxey & Riley 1983). These include the Archimedes force, added mass, Basset force, components of lift force and various smaller terms (e.g. Faxen corrections). The added mass and Basset forces are related to fluid and particle accelerations and to the time evolution of the relative motion. Although closure expressions for these forces can be found in the literature, we ignore them as there is no clear directional bias to these contributions. Similarly, we ignore the Magnus component of the lift force, which is related to systematic rotation of solid particles. The leading-order Archimedes force is likely to be transverse to the main flow direction, driven by streamline curvature (see below). There has been considerable work on the lift forces experienced by particles in shear flows at moderate *Re* (e.g. Hogg 1994; Asmolov 1999; Asmolov, Lebedeva & Osipov 2009; Asmolov &

Osipov 2009; Lebedeva & Asmolov 2011), with the last specifically focused on fracturing. These studies do require small particle Reynolds numbers and are aimed at dilute suspensions. Although this limits the accuracy of applying these closures directly, they are valuable in assessing the magnitude of the lift force. In particular, when the principal components of the velocity are in the plane of the fracture, the main lift force components acts transversely, in the  $y$ -direction. In summary, the main contributions to  $f_D$  will be in the  $y$ -direction, which means that the main contribution to  $(f_{D,x}, f_{D,z})$  comes from the term  $\delta_p^2 \phi Re / Fr^2$ , aligned with gravity.

The solid-phase  $y$ -momentum balance is important in that the particle forces here contribute to the diffusive particle fluxes:

$$\underbrace{O(\delta_t^2 Re)}_{IT} = \delta_t Re s \phi \frac{u_{s,str}^2}{r_\kappa} - \lambda_y \frac{\partial \Pi}{\partial y} + \frac{f_{D,y} + f_{D',y}}{\delta_p^2} + \underbrace{O(\delta_t)}_{CT} + \underbrace{O(\delta_t)}_{SSG}, \tag{3.20}$$

with the same meaning as before, regarding the terms identified as  $CT$  and  $SSG$ . The terms marked  $IT$  in (3.20) are inertial terms of the specified order. At lower order (moved to the right-hand side) is a centrifugal term that may become important in cases where the fracture has streamwise curvature: here the scaled radius of curvature is  $r_\kappa$  and  $u_{s,str}$  indicates the solids-phase speed in the local  $(x, z)$ -plane, along the fracture. As commented above, the two leading-order terms in  $f_{D',y}$  that have a consistent directional bias are a transverse Archimedes force and lift force. The transverse Archimedes force is similar to the centrifugal term but involves the fluid density and speed in the local  $(x, z)$ -plane. Combining this with the centrifugal term in (3.20) leads to

$$f_{A,y} \approx \delta_p^2 \delta_t Re (s - 1) \phi \frac{u^2 + w^2}{r_\kappa}, \tag{3.21}$$

with relative error of the size of the relative velocity. We denote the scaled lift forces by  $f_{L,y}$  and note simply that prescribing  $f_{L,y}$  fully is not possible from the current literature. The expressions deriving from Hogg (1994) and Asmolov (1999) and similar relate to Newtonian fluids and dilute regimes. Recent studies by Lashgari *et al.* (2014, 2016) show that lift affects the particle distribution only at smaller solid volume fractions (see also Segre & Silberberg (1961)): for  $\phi > 0.2$ , the particle distribution is governed increasingly by particle–particle interactions and particle-phase stress.

In summary, from (3.20) we find that

$$f_{D,y} = \delta_p^2 \lambda_y \frac{\partial \Pi}{\partial y} - f_{A,y} - f_{L,y} + O(\delta_p^2 \delta_t) + O(\delta_p^2 \delta_t^2 Re). \tag{3.22}$$

In substituting for the relative velocity in (2.16), we will take the divergence of the relative velocity. Owing to the scaling, the  $y$ -derivative in the divergence operator is multiplied by  $1/\delta_t$ . Thus, in neglecting small terms in  $f_{D,y}$ , to be consistent with the  $(x, z)$ -directions we should neglect only the terms of  $O(\delta_p^2 \delta_t)$  and  $O(\delta_p^2 \delta_t^2 Re)$ . We cannot say whether or not the lift and Archimedes terms are consistently smaller/larger than the stress gradient term. In all likelihood there will be parameter regimes where these forces are significant, e.g. tortuous fractures at high speeds for  $f_{A,y}$  and dilute regimes for  $f_{L,y}$ . We continue by assuming that the three contributions to  $f_{D,y}$  are comparable in (3.22). Note, however, that we have neglected terms that are strictly

$O(\delta_p^2)$  in estimating  $f_{D,x}$  and  $f_{D,z}$ , retaining only the term  $\delta_p^2 \phi Re / Fr^2$ . Consistent with this approximation is that the magnitude of the drag force vector does not involve  $f_{D,y}$  at leading order, i.e. at leading order we have  $|f_D| = \delta_p^2 \phi Re / Fr^2$  and consequently

$$\mathbf{u}_r \approx -M \left( \left| \frac{\delta_p^2 \phi Re}{Fr^2} \right| \right) \left( 0, \delta_p^2 \lambda_y \frac{\partial \Pi}{\partial y} - f_{A,y} - f_{L,y}, -\delta_p^2 \frac{Re}{Fr^2} \phi \right). \tag{3.23}$$

The leading-order relative velocities are now inserted into the solids mass conservation law:

$$\begin{aligned} \frac{\partial \phi}{\partial t} + \nabla \cdot [\phi \mathbf{u}] &= \frac{\delta_p^2}{\delta_t} \frac{\partial}{\partial y} \left[ \phi(1 - \phi) M \left( \left| \frac{\delta_p^2 \phi Re}{Fr^2} \right| \right) \left( \lambda_y \frac{\partial \Pi}{\partial y} - \frac{f_{L,y} + f_{A,y}}{\delta_p^2} \right) \right] \\ &+ \frac{\delta_p^2 Re}{Fr^2} \frac{\partial}{\partial z} \left[ \phi^2(1 - \phi) M \left( \left| \frac{\delta_p^2 \phi Re}{Fr^2} \right| \right) \right]. \end{aligned} \tag{3.24}$$

Finally, the granular temperature equation scales as follows:

$$\begin{aligned} 0 &= \eta_f \eta_s(\phi, \Theta) [u_y^2 + w_y^2] - 12 \eta_f \alpha(\phi, \Theta) \Theta + \delta_p^2 \frac{\partial}{\partial y} \left[ 3 \eta_f \kappa(\phi, \Theta) \frac{\partial \Theta}{\partial y} \right] \\ &- \delta_p^2 \delta_t Re s \phi C(\phi) \frac{D_p \Theta}{Dt} + \underbrace{O(\delta_p^2 \delta_t^2)}_{HFT} + \underbrace{O(\delta_t^2)}_{VDT}, \end{aligned} \tag{3.25}$$

where neglected terms are lower-order terms in the heat flux (*HFT*) and viscous dissipation functional (*VDT*). The convective terms are small and to leading order the balance is simply

$$0 = \eta_f \eta_s [u_y^2 + w_y^2] - 12 \eta_f \alpha(\phi, \Theta) \Theta + \delta_p^2 \frac{\partial}{\partial y} \left[ 3 \eta_f \kappa(\phi, \Theta) \frac{\partial \Theta}{\partial y} \right]. \tag{3.26}$$

As in Nott & Brady (1994) the heat flux term is largely inactive unless we have large gradients in  $\Theta$ .

### 3.2. Viable modelling frameworks

The  $(x, z)$ -domain has size  $L \times H$ . We regard  $\delta_t$  as characteristic of streamwise geometrical variations. The principal equations are (3.13)–(3.16), (3.24) and (3.26), with all terms *CT* and *SSG* neglected. Evidently, if we consider all  $O(\delta_t)$  terms, we invite suffocating geometric complexity, quite apart from the additional normal stresses and shear stress contributions. Neglecting terms strictly of  $O(\delta_t)$ , we see that the Hele-Shaw type of model is recovered as  $\delta_t \rightarrow 0$  at fixed  $Re$ . If  $Re$  is  $O(1)$ , then anyway the Hele-Shaw type of averaging is valid, but in practice many fracturing flows have large  $Re$ . Insofar as the bulk suspension flow is concerned, the terms of  $O(\delta_t Re)$  are probably the most important to include at high flow rates. These terms change the form of the momentum balance. Equally, at higher flow rates we would expect larger gradients in shear rates and thus inertial effects to appear at the particle scale in sheared layers nearer the walls. In summary, it appears that two types of model are feasible within this framework, according partly to the fracture geometry, fluid rheology and flow rates.

3.2.1. Long thin uniform fractures

Here we effectively assume that  $\delta_t \sim 1/L$ , that  $Re$  is moderate and that the fracture width  $\hat{D}$  is small enough for  $\delta_p^2 \gg \delta_t$ . The following model equations result:

$$0 = \nabla \cdot \mathbf{u}, \tag{3.27}$$

$$0 = -\frac{\partial p_f}{\partial x} + \frac{\partial}{\partial y} \left[ \eta_f [1 + \eta_s] \frac{\partial u}{\partial y} \right], \tag{3.28}$$

$$0 = -\frac{\partial p_f}{\partial y}, \tag{3.29}$$

$$0 = \frac{Re}{Fr^2} \phi - \frac{\partial p_f}{\partial z} + \frac{\partial}{\partial y} \left[ \eta_f [1 + \eta_s] \frac{\partial w}{\partial y} \right], \tag{3.30}$$

$$\begin{aligned} \frac{\partial \phi}{\partial t} = & -\nabla \cdot [\phi \mathbf{u}] + \frac{\delta_p^2}{\delta_t} \frac{\partial}{\partial y} \left[ \phi(1 - \phi) M \left( \left| \frac{\delta_p^2 \phi Re}{Fr^2} \right| \right) \left( \lambda_y \frac{\partial \Pi}{\partial y} - \frac{f_{L,y} + f_{A,y}}{\delta_p^2} \right) \right] \\ & + \frac{\delta_p^2 Re}{Fr^2} \frac{\partial}{\partial z} \left[ \phi^2(1 - \phi) M \left( \left| \frac{\delta_p^2 \phi Re}{Fr^2} \right| \right) \right], \end{aligned} \tag{3.31}$$

$$0 = \eta_f \eta_s [u_y^2 + w_y^2] - 12\eta_f \alpha(\phi, \Theta) \Theta + \delta_p^2 \frac{\partial}{\partial y} \left[ 3\eta_f \kappa(\phi, \Theta) \frac{\partial \Theta}{\partial y} \right]. \tag{3.32}$$

This model has potential for further analysis and is continued below in § 4, where we shall neglect  $f_{L,y}$  and  $f_{A,y}$  for simplicity.

3.2.2. Inertial hydraulics in rough fractures

A second set of equations that it makes sense to consider involve more geometrically complex fractures, where  $\delta_t \gg 1/L$ , higher flow rates and lower viscosities are considered. Inertial terms would need modelling in the momentum balance. These flows are likely to have a modified velocity profile from that which results from the long thin model above, as physically the geometry prevents the flow from ever fully developing; see e.g. the computations of Skjetne *et al.* (1999) for a Newtonian flow. This unsteadiness may warrant incorporation of an additional diffusive term in the solids-phase mass conservation equation.

Computationally, this type of model still benefits from being reduced with respect to a full Navier–Stokes problem, but would need resolving as the flow evolves along the fracture. Effectively, the Navier–Stokes system is reduced to a set of boundary layer-type equations. The solids-phase mass conservation equation now does not necessarily evolve to a dispersive limit. This model framework requires considerable development, in both modelling and computation. Although such a model is needed for inertial flows in spatially varying fractures, note that, if developed, this model should incorporate all the dynamics of the model in § 3.2.1, which is anyway a limiting case.

4. Analysis of flows in long thin uniform fractures

In the remainder of the paper we explore the model in § 3.2.1. We note that the momentum and temperature balances are stationary, driven by time variations in  $\phi$  solved by integrating forward (3.31). It is worth mentioning that recently Dontsov & Peirce (2014) and Lecampion & Garagash (2014) have studied the leading-order Stokesian flows of Newtonian slurries in long thin uniform fractures. Our analysis extends beyond this by considering inertial flows of non-Newtonian slurries in

the presence of gravitational effects in both leading order and first order, and in developing a general framework. Particularly, our main interest is in the streamwise development of the suspension properties along the fracture.

We consider first the limit  $\delta_t/\delta_p^2 \ll 1$  of rapid transverse equilibrium. The physical meaning of this limit can be heuristically explained as follows. The advective time scale along the fracture is  $\hat{t}_a \sim \hat{L}_t/\hat{U}_0$ . Solids-phase diffusivity, on the other hand, scales with  $\hat{\gamma}\hat{d}_p^2$ , so that the time scale for equilibration across the fracture is  $\hat{t}_d = \hat{D}^2/(\hat{\gamma}\hat{d}_p^2)$ . Therefore, the ratio of these time scales is

$$\frac{\hat{t}_d}{\hat{t}_a} \sim \frac{\hat{D}^2\hat{U}_0}{\hat{\gamma}\hat{d}_p^2\hat{L}_t} = \frac{\delta_t}{\delta_p^2}. \tag{4.1}$$

In other words, the limit  $\delta_t/\delta_p^2 \ll 1$  corresponds to that in which a rapid transverse equilibrium of the solids distribution is attained over a length scale that is shorter than  $\hat{L}_t$ . For simplicity, and since we do not have adequate closure models, we ignore the terms  $f_{L,y}$  and  $f_{A,y}$  for the remainder of the paper. We also approximate  $\phi Re/Fr^2$  by  $\bar{\phi} Re/Fr^2$  in (3.30), where  $\bar{\phi}$  is the value of  $\phi$  averaged across the fracture, i.e. assume the local distribution of  $\phi$  has a secondary influence on determining the velocity field, in terms of the distribution of buoyancy forces (but not in terms of viscous effects); see appendix B for a discussion of this. This implies that the velocity vector in the plane of the fracture,  $(u, w)$ , is parallel to the modified pressure gradient:

$$(u, w) \parallel \left( -\frac{\partial p_f}{\partial x}, -\frac{\partial p_f}{\partial z} + \frac{Re}{Fr^2}\bar{\phi} \right). \tag{4.2}$$

We orient the coordinates in the direction  $\xi$ , parallel to  $(u, w)$ , to evaluate the leading-order streamwise dispersion. Therefore, (3.28)–(3.30) are replaced by a single momentum equation for the streamwise velocity, parametrized at each location by the distribution of  $\phi, \Theta$ . Time evolution occurs only via (3.31).

Defining  $\varepsilon = \delta_t/\delta_p^2 \ll 1$ , we seek an approximation to  $\phi$  and the other variables using a regular asymptotic expansion in  $\varepsilon$ , i.e.

$$U = U_0 + \varepsilon U_1 + \dots, \quad \phi = \phi_0 + \varepsilon \phi_1 + \dots, \quad \Theta = \Theta_0 + \varepsilon \Theta_1 + \dots, \quad \text{etc.} \tag{4.3a-c}$$

We substitute the above into (3.27)–(3.32) and collect terms of the same order. Note that  $U$  here is in the direction of the streamlines, which are not themselves evaluated in this simple model, i.e. we look at evolution along a streamline.

*Zeroth-order problem:*

At leading order we have

$$0 = \frac{\partial U_0}{\partial \xi} + \frac{\partial v_0}{\partial y}, \tag{4.4}$$

$$|G|y = \left[ \eta_f[1 + \eta_s] \frac{\partial U_0}{\partial y} \right], \quad |G| = \left| \left( \frac{\partial p_f}{\partial x}, \frac{\partial p_f}{\partial z} - \frac{Re}{Fr^2}\bar{\phi} \right) \right|, \tag{4.5a,b}$$

$$0 = -\frac{\partial p_{0f}}{\partial y}, \tag{4.6}$$

$$0 = \frac{\partial}{\partial y} \left[ \phi_0(1 - \phi_0)M \left( \left| \frac{\delta_p^2 \phi_0 Re}{Fr^2} \right| \right) \lambda_y \frac{\partial \Pi_0}{\partial y} \right], \tag{4.7}$$

$$0 = \eta_f \eta_s \left[ \frac{\partial U_0}{\partial y} \right]^2 - 12 \eta_f \alpha_0(\phi_0) \Theta_0, \tag{4.8}$$

with boundary conditions  $U_0 = 0$  at  $y = \mp y_{w,\mp}(x, z)$ . Note that  $|G|$  here is independent of  $y$ . In practice we may know the local mean speed, say  $\bar{U}_0$ , and the local average solids fraction,  $\bar{\phi}_0$ . Thus, two additional constraints are

$$\bar{U}_0 = \int_{-y_{w,-}}^{y_{w,+}} U_0 \, dy, \tag{4.9}$$

$$\bar{\phi}_0 h_w(x, z) = \int_{-y_{w,-}}^{y_{w,+}} \phi_0 \, dy, \tag{4.10}$$

where  $h_w(x, z) = [y_{w,+}(x, z) + y_{w,-}(x, z)]$  is the local fracture width. The coupled system of equations (4.5)–(4.10) can be solved to obtain  $|G|$ ,  $U_0(y)$ ,  $\phi_0(y)$  and  $\Theta_0(y)$ . The form of the equations guarantees a unique solution for specified mean velocity and mean volume fraction; see §4.1.

*First-order problem:*

At first order we use only the solids mass conservation equation:

$$\frac{\partial \phi_0}{\partial t} + U_0 \frac{\partial \phi_0}{\partial \xi} + v_0 \frac{\partial \phi_0}{\partial y} = \frac{\partial}{\partial y} \left[ \phi_0 (1 - \phi_0) M \left( \left| \frac{\delta_p^2 \phi_0 Re}{Fr^2} \right| \right) \lambda_y \frac{\partial \Pi_1}{\partial y} \right]. \tag{4.11}$$

We integrate (4.11) across the width of the fracture and use (4.4) to get

$$0 = \int_{-y_{w,-}}^{y_{w,+}} \frac{\partial \phi_0}{\partial t} \, dy + \int_{-y_{w,-}}^{y_{w,+}} \frac{\partial}{\partial \xi} U_0 \phi_0 \, dy, \tag{4.12}$$

which can be written as

$$0 = \frac{\partial}{\partial t} [h_w \bar{\phi}_0] + \frac{\partial}{\partial \xi} [h_w (F(\bar{\phi}_0, \bar{U}_0) + \bar{U}_0 \bar{\phi}_0)]. \tag{4.13}$$

The flux  $F$  is defined as

$$F(\bar{\phi}_0, \bar{U}_0) = \frac{1}{h_w} \int_{-y_{w,-}}^{y_{w,+}} \tilde{U}_0(y) \tilde{\phi}_0(y) \, dy, \tag{4.14}$$

$$U_0 = \bar{U}_0 + \tilde{U}_0(y), \quad \phi_0 = \bar{\phi}_0 + \tilde{\phi}_0(y), \tag{4.15a,b}$$

which we note is a form of covariance or correlation between  $\tilde{U}_0$  and  $\tilde{\phi}_0$ .

The form of first-order problem (4.13) is quite general. The characteristics of the leading-order distributions of  $U_0$  and  $\phi_0$  determine the type of leading-order transport. We can continue the asymptotic approximation to the next order to derive an advection–diffusion equation for the slow-time evolution of  $\phi_0$ . This next-order diffusive term is effectively the Taylor dispersion. For example, such an approach was followed recently in Ramachandran (2013) for flows of Newtonian suspensions modelled by Stokesian SBM. Whether or not the diffusive terms govern proppant dispersion depends on the first-order flux. As we shall see below, the leading-order distributions of  $\phi_0$  show significant transverse variation and generally the flux  $F(\bar{\phi}_0, \bar{U}_0)$  is non-zero. Thus, the dominant contribution to spreading comes at first order and we do not extend the analysis deeper here.



4.1. Computation of  $F(\bar{\phi}_0, \bar{U}_0)$

Our leading-order model is based on the conservation law (4.13), which is governed by  $F(\bar{\phi}_0, \bar{U}_0)$ . In order to construct  $F$ , let us assume that  $\bar{\phi}_0$  and  $\bar{U}_0$  are given. If we integrate (4.7) once and impose a symmetry condition on  $\Pi_0$  at  $y = 0$ , we see that  $\Pi_0$  is constant across the fracture. Thus, we have three variables to find,  $U_0(y)$ ,  $\phi_0(y)$ ,  $\Theta_0(y)$ , as well as two constants, the pressure gradient  $|G|$  and the leading-order solids pressure  $\Pi_0$ .

To solve our nonlinear system of three variables and two constants, we first note that (4.8) relates  $\Theta_0$  algebraically to  $\phi_0$  and  $|U'_0|$  (denoting the  $y$ -derivative of  $U_0(y)$ ). It may be verified that this expression has a unique solution for given  $|U'_0|$  and  $\phi_0 \in [0, \phi_m)$ . Thus, below, we assume that  $\Theta_0$  is a known function of  $|U'_0|$  and  $\phi_0$ . Since we have  $\Pi_0 = \text{const.}$ , we set this value from values at  $y = 0$ , i.e. we use

$$\Pi_0 = (\eta_f \Theta_0^{1/2} p) \Big|_{y=0}. \tag{4.16}$$

This uniquely defines  $\Pi_0$  in terms of the centreline value of  $\phi_0$ , i.e.  $\phi_0(0)$ . On evaluating  $\Pi_0$  in this way, we may then calculate  $\phi_0(y)$  across the fracture, with the distribution depending only on  $\phi_0(0)$  and  $|U'_0|$ .

Next, for any  $(\phi_0, \Theta_0)$  with  $\phi_0 \in [0, \phi_m]$ , the function  $\eta_f [1 + \eta_s] |U'_0|$  is strictly monotone with respect to the velocity gradient  $|U'_0|$ . This is effectively the flow curve (constitutive law) of the suspension under steady shear. As discussed above,  $(\phi_0, \Theta_0)$  are themselves determined by  $|U'_0|$  and  $\phi_0(0)$ .

Thus, for given  $|G|$  and  $\phi_0(0)$ , (4.5) uniquely determines the velocity gradient at each  $y$ . We now iterate with respect to  $\phi_0(0)$  at fixed  $|G|$  in order to satisfy (4.10). Finally, on integrating out from the wall,  $U_0(y)$  is determined from  $|U'_0|(y)$ , and a further integration yields the flow rate. The applied pressure gradient  $|G|$  is adjusted in order to satisfy the flow rate constraint (4.9).

The various nonlinear equations to be solved are either algebraically solved, or involve monotone continuous functions, for which various robust root-finding procedures can be used. We regularize the relative viscosity to remove the singular behaviour of  $\eta_r(\phi_0)$  as  $\phi_0 \rightarrow \phi_m^-$ . The relative viscosity is regularized as

$$\eta_r(\phi) = (1 - \phi/\phi_m + \epsilon)^{-2.5\phi_m}, \tag{4.17}$$

where  $\epsilon$  is the regularization parameter. The results of this paper are invariant for  $\epsilon \leq 10^{-5}$ . The equations are then solved iteratively in the nested fashion indicated in the above description, i.e.  $|G| \rightarrow U_0(y) \rightarrow \phi_0(0) \rightarrow \phi_0(y) \rightarrow \Theta_0(y)$ . Finally, having computed  $U_0(y)$  and  $\phi_0(y)$ , we subtract  $\bar{U}_0$  and  $\bar{\phi}_0$ , respectively, and integrate (4.14) to give  $F(\bar{\phi}_0, \bar{U}_0)$ .

4.1.1. Example results

To illustrate the main parametric variations of the flux function and associated zeroth-order model, we consider a simple scenario of a uniform fracture (hence  $y_{w,\pm} = 1/2$  and  $h_w = 1$ ). We assume a local mean velocity  $\bar{U}_0 = 1$  and explore variations about a representative set of dimensionless parameters:  $Re = 10$ ,  $B = 1$ ,  $n = 0.5$ ,  $Fr = 1$ ,  $s = 2.65$ ,  $\delta_p = 0.05$  and  $\delta_t = 0.0001$  (and, where needed,  $\phi_{in} = \phi_0 = 0.5$ ). Keeping this base set of parameters fixed, we compute  $F(\bar{\phi}_0) = F(\bar{\phi}_0, 1)$ , and the zeroth-order solution variables, by individually varying the Bingham number  $B = 1, 2, 4, 6, 8, 10$ , the power-law index  $n = 0.3, 0.4, 0.5, 0.6, 0.7, 1.0$  and the Reynolds number  $Re = 1, 10, 100, 200, 400$ .

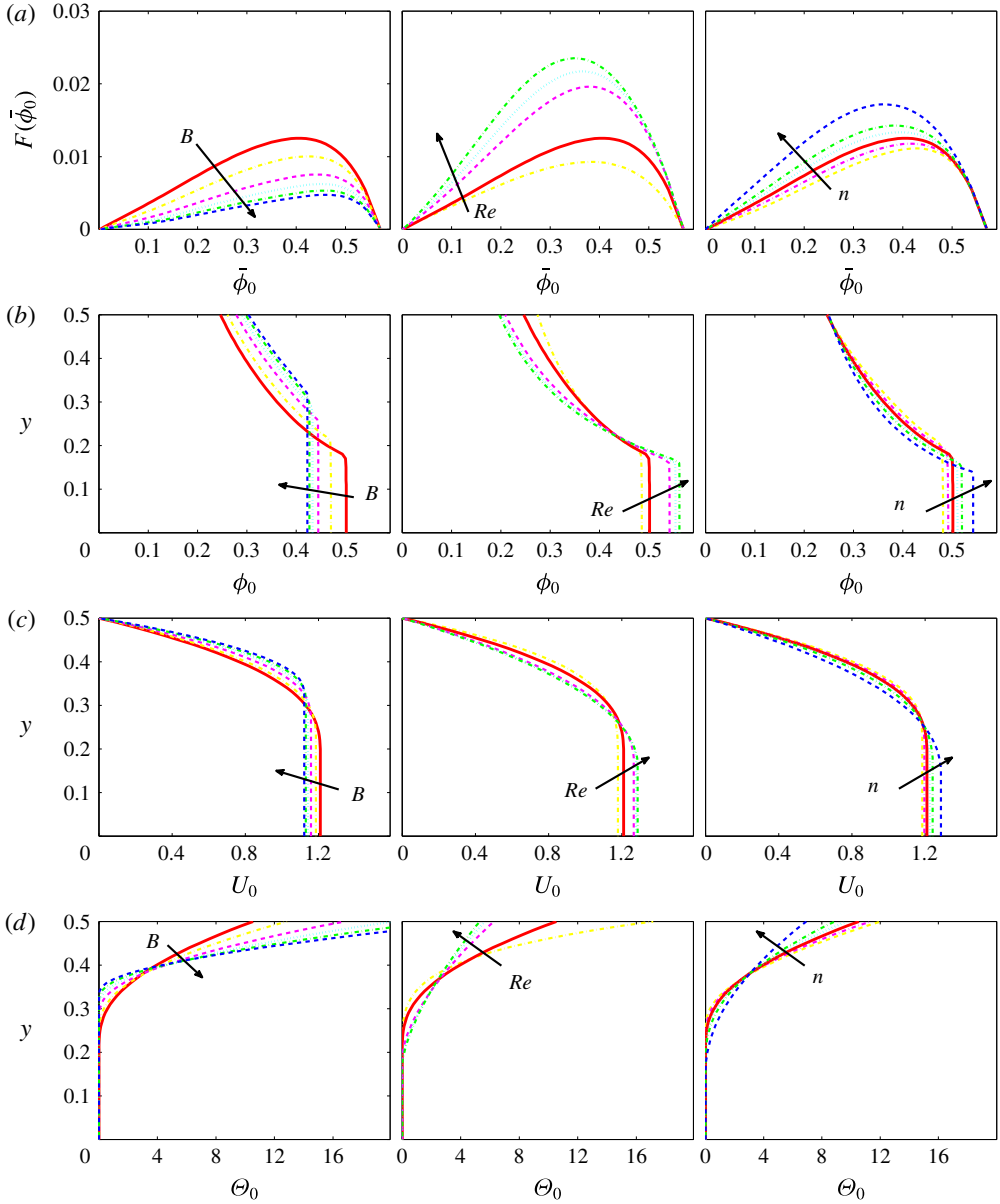


FIGURE 3. (Colour online) Flux function for a range of flow parameters:  $B = 1, 2, 4, 6, 8, 10$ ,  $Re = 1, 10, 100, 200, 400$  and  $n = 0.3, 0.4, 0.5, 0.6, 0.7, 1.0$ . The solid red line corresponds to a representative set of dimensionless parameters:  $Re = 10$ ,  $B = 1$ ,  $n = 0.5$ ,  $Fr = 1$ ,  $s = 2.65$ ,  $\delta_p = 0.05$  and  $\delta_t = 0.0001$ . The flow profiles are associated with the case of  $\bar{\phi}_0 = 0.4$ .

Figure 3 shows the results. Figure 3(a) indicates the computed flux function under each parameter variation. Note here that  $\bar{\phi}_0$  varies between 0 and  $\phi_m = 0.57$ . Increasing  $B$  tends to reduce the amplitude of  $F(\bar{\phi}_0)$  and skew the flux function towards higher

concentrations. Intuitively, larger  $B$  results in a more uniform velocity that reduces  $\tilde{U}_0$ , but we also find a contributing reduction in  $\tilde{\phi}_0$ .

The reverse effect is found for increasing  $Re$ , which increases the amplitude of  $F(\tilde{\phi}_0)$  and increases axial dispersion. However, the increase in  $Re$  also results in a more symmetric  $F(\tilde{\phi}_0)$ . These changes are again attributable to increases in the amplitudes of  $\tilde{U}_0$  and  $\tilde{\phi}_0$ . Similarly, increasing  $n$  results in increased amplitude and symmetry of  $F(\tilde{\phi}_0)$ . Since the conservation law (4.13) is a quasi-linear first-order equation, the qualitative behaviour is governed by the derivative  $F'(\tilde{\phi}_0)$  and by the heights of kinematic shocks that will result. These are highly dependent on the shape of  $F(\tilde{\phi}_0)$ . Examples of the variations in the base solution are presented in figure 3(b–d) for the case  $\bar{\phi}_0 = 0.4$ . The results for  $\phi_0(y)$  show that particles migrate towards the centre of the fracture where the pseudo-plug exists and where  $\phi_0(y)$  approaches a critical volume fraction  $\phi_c \neq \phi_m$ .

Interestingly, we have not considered at leading order the conductive term in the particle temperature equation. In the Newtonian SBM channel flow, this term is critical in keeping a small non-zero  $\Theta_0$  at the channel centre, which acts to regularize and remove the cusp that otherwise results. There is a different form of regularization in our model, within the pseudo-plug region: namely, we have assumed a limiting strain rate of  $\sim \delta_r$  due to axial variation along the fracture. Although this term would act to smooth  $\phi_0(y)$  at the centre, this is not the reason for  $\phi_0(y) \sim \phi_c < \phi_m$  in the pseudo-plug, as we now explain.

Having  $\phi_c < \phi_m$  by a finite amount is consistent with the recent rheological results of Dagois-Bohy *et al.* (2015), which explored the constitutive laws of non-colloidal particles in yield stress fluids. Using the frictional viewpoint, it is shown that the effective friction and the solid volume fraction depend on two dimensionless parameters,  $J = \hat{\eta} \hat{\gamma}^n / \hat{P}$  and  $J_y = \hat{\tau}_Y / \hat{P}$ . For a constant  $J_y$ , the volume fraction was found not to approach  $\phi_m$  as  $J \rightarrow 0$  (controlled via vanishing  $\hat{\gamma}$ ). Instead, it was shown that  $\phi$  approaches a volume fraction  $\phi_c < \phi_m$  that depends on  $J_y$ . However,  $\phi_m$  can be approached by  $\phi_c$  in the limit of  $J_y \rightarrow 0$ , i.e. vanishing yield stress.

In our results, we have the leading-order particle pressure constant across the fracture and hence also  $J_y$ . Both the  $J_y$  and  $J$  from Dagois-Bohy *et al.* (2015) are included in our  $J$ , introduced earlier, as our local viscosity includes both viscous shear-thinning and yield stress terms. As we enter the pseudo-plug the viscous term approaches zero and therefore only the constant  $J_y$  remains. As with Dagois-Bohy *et al.* (2015), the solid volume fraction does not approach  $\phi_m$  in the pseudo-plug or at the centre. The physical interpretation is that the particle pressure balances with the yield stress, limiting further migration. An interesting observation is that, as we increase the yield stress of the suspending fluid, the final solid volume fraction (in the limit of zero shear rate) decreases. This suggests that even a finite confining pressure cannot break the unyielded plug regions forming between the particles resisting the squeezing motions. We are currently studying this problem experimentally. The hypothesis is that compaction does not occur in the case of a suspending yield stress fluid and that the usual jamming fraction is not approached (see Firouznia *et al.* 2016).

Recently Lecampion & Garagash (2014) developed a model for confined flows of neutrally buoyant Newtonian suspensions based on frictional rheology. Basically, the authors extended the framework presented by Boyer, Boyer & Pouliquen (2011) to achieve the fully jammed state (the random close-packing limit) in the limit of zero shear rate when the shear-induced migration of particles occurs. Formation of a Bingham-like plug in Newtonian suspensions is further studied by Ahnert, Münch &

Wagner (2014) from a two-phase flow perspective. Later Oh *et al.* (2015) carried out experimental measurements of the solid volume fraction in a pipe configuration for flows of neutrally buoyant Newtonian suspensions and showed that the fully jammed state is achievable in the central region of the pipe. As pointed out by Oh *et al.* (2015), the underlying mechanism associated with the compaction in the plug region (meaning the region in which  $\phi$  approaches  $\phi_m$  in Newtonian suspensions) can be related to microscopic particle rearrangements caused by velocity fluctuations of the particles. Potentially, the yield stress prevents these fluctuations, accounting for the different plug behaviour.

The effects of varying  $B$ ,  $Re$  and  $n$  on  $\Theta_0(y)$  are illustrated in figure 3(d). In general  $\Theta_0(y)$  drops to close to zero within the pseudo-plug, but is certainly significant in the shear layers close to the walls. The maximal  $\Theta_0(y)$  is found at the wall and is observed to increase with  $B$ , but to decrease with both  $Re$  and  $n$ .

#### 4.2. Proppant propagation

To study proppant propagation behaviour, we solve (4.13) numerically for a given  $F(\bar{\phi}_0)$  under different operational scenarios. This is a first-order quasi-linear hyperbolic equation, for which many numerical methods exist. Here we have used a second-order extension of the staggered Lax–Friedrichs scheme introduced by Nessyahu & Tadmor (1990) with Superbee limiter (see Leveque 2002). The implementation has been tested with a range of test problems, omitted here for brevity. In fact, for the numerical integration, we use an interpolated  $F(\bar{\phi}_0)$  evaluated by solving for  $F$  at a number of discrete values. Here we use spacing  $\delta\bar{\phi}_0 \approx 0.01$ .

##### 4.2.1. Spreading of a single slug of proppant

Consider flow of a yield stress fluid pumped continuously at the inlet of a fracture. At times  $t > t_0$ , proppant with volume fraction  $\bar{\phi}_0$  is added at the fracture inlet for a time period  $T$  and then turned off, leaving a single slug of proppant to advect and spread along the fracture. Figure 4 shows the spreading and flow profiles for a typical fracturing flow with parameters  $Re = 100$ ,  $B = 1$ ,  $n = 1.0$ ,  $Fr = 1.44$ ,  $s = 2.65$ ,  $\delta_p = 0.03$  and  $\delta_t = 0.0001$ . A single slug of proppant with  $\bar{\phi}_0 = 0.5$  is added to the flow at the fracture inlet for a time period  $T = 0.1$ . The computed flux function is shown in figure 4(a). According to (4.13) the streamwise spreading speed is equal to the wave speed, which is  $1 + \partial F(\bar{\phi}_0)/\partial \bar{\phi}_0$ . The minimum wave speed is at  $\bar{\phi}_0 = \phi_m$ . The maximum wave speed is somewhere above  $\bar{\phi}_0 = 0$ , as  $F(\bar{\phi}_0)$  appears to be convex close to  $\bar{\phi}_0 = 0$ .

On analysing  $\partial F(\bar{\phi}_0)/\partial \bar{\phi}_0$  we deduce that the slug should spread at the front and steepen at the back, which is indeed found in figure 4(b), which shows the streamwise dispersion of mean solid volume fraction. Also shown in figure 4(c) is the scaled length of the slug,  $L_s$ , which is proportional to the difference in wave speeds at the front and back of the slug (denoted by  $\phi_f$  and  $\phi_b$ , respectively),

$$\frac{L_s}{L_t} = \left[ \frac{\partial F(\bar{\phi}_0)}{\partial \bar{\phi}_0} \Big|_{\phi_f} - \frac{\partial F(\bar{\phi}_0)}{\partial \bar{\phi}_0} \Big|_{\phi_b} \right] t. \quad (4.18)$$

Note that  $\phi_f$  and  $\phi_b$  can be calculated directly from  $F(\bar{\phi}_0)$ . Figure 4(c) shows the expected linear growth of the slug length with time.

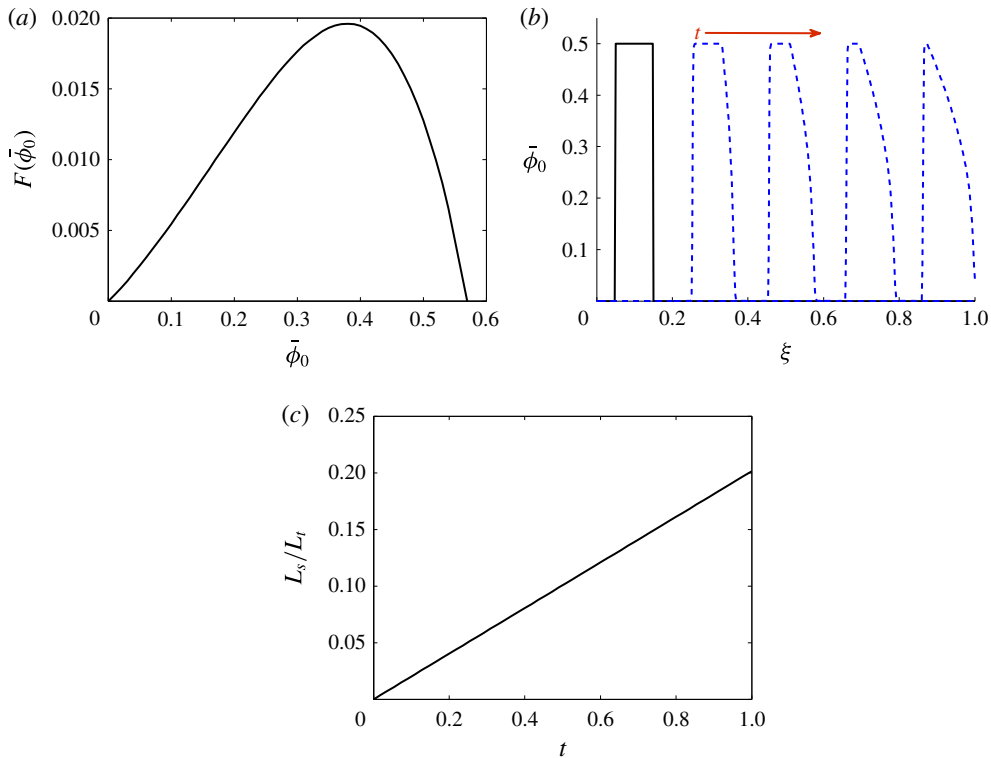


FIGURE 4. (Colour online) Single slug of proppant for  $Re = 100$ ,  $B = 1$ ,  $n = 1.0$ ,  $Fr = 1.44$ ,  $s = 2.65$ ,  $\delta_p = 0.03$ ,  $\delta_t = 0.0001$  and  $\bar{\phi}_m = 0.5$ , of duration  $T = 0.1$ : (a) flux function; (b)  $\bar{\phi}_0(\xi, t)$  at regular time intervals; (c) ratio of spreading length to streamwise length scale.

As the entire leading-order solution is determined by average velocity and solids fractions (see the computational procedure in § 4.1), we are in a position to reconstruct the distribution of solids across the fracture at each  $(y, \xi, t)$ . Snapshots of the solids fraction  $\phi_0(y, \xi, t)$  are plotted in the left-hand column of figure 5 at successive times. We see that the maximum solid volume fraction occurs in the pseudo-plug region, but that a solids-depleted region exists on the top right corner of the slug, i.e. at the front closest to the wall. As noted previously, the maximum solid volume fraction remains below  $\phi_m$ .

Although sedimentation does not affect the leading-order transport equation for  $\bar{\phi}_0$ , hindered settling velocities can be estimated from (2.19) and (2.20), post-processed from the leading-order solution. This is shown in the right-hand column of figure 5. The colour maps of scaled sedimentation velocity in the  $(\xi, y)$  plane have been normalized using a sedimentation velocity that is calculated for  $\bar{\phi}_0 = \phi_m = 0.5$  and for the maximal inlet shear rate. We observe that the sedimentation velocity is almost zero in the pseudo-plug region, but can be significantly larger in the depleted regions near the wall, which correspond to the regions of lowest fluid viscosity within the slug. Note, lastly, that, outside the slug, where  $\phi_0(y, \xi, t) = 0$ , there is no sedimentation.

Returning now to figure 4(c) and the estimates of normalized slug length, we now explore how the scaled dispersion length of the slug at the end of the fracture varies.

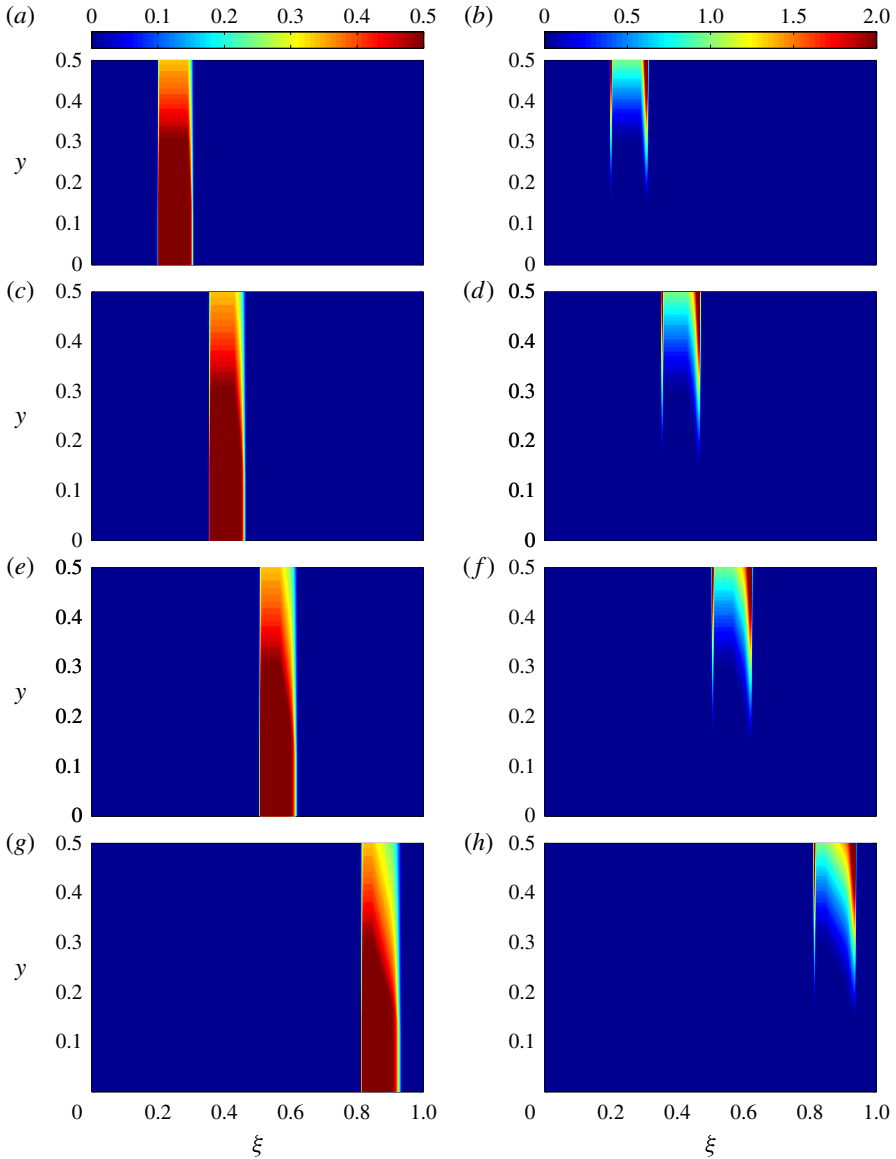


FIGURE 5. (Colour online) (a,c,e,g) Colour maps of  $\phi_0(y, \xi, t)$  as the single proppant slug propagates. (b,d,f,h) Colour maps of scaled sedimentation velocity as the single pulse propagates. The sedimentation velocity is scaled with the sedimentation velocity of  $\phi_0 = 0.5$  at the maximum shear rate of the inflow. The representative set of dimensionless parameters are:  $Re = 10$ ,  $B = 1$ ,  $n = 0.5$ ,  $Fr = 1$ ,  $s = 2.65$ ,  $\delta_p = 0.05$  and  $\delta_t = 0.0001$ .

Figure 6 takes the same base parameter set as for figure 4, varying each of  $B$ ,  $Re$  and  $n$ . It is evident that increasing the yield stress through the Bingham number limits the dispersion. Also, we see that dispersion is an increasing function of  $Re$  number and  $n$ . This confirms our basic intuition regarding dispersion being controlled by flatter velocity profiles, governed rheologically by  $(B, n)$ .

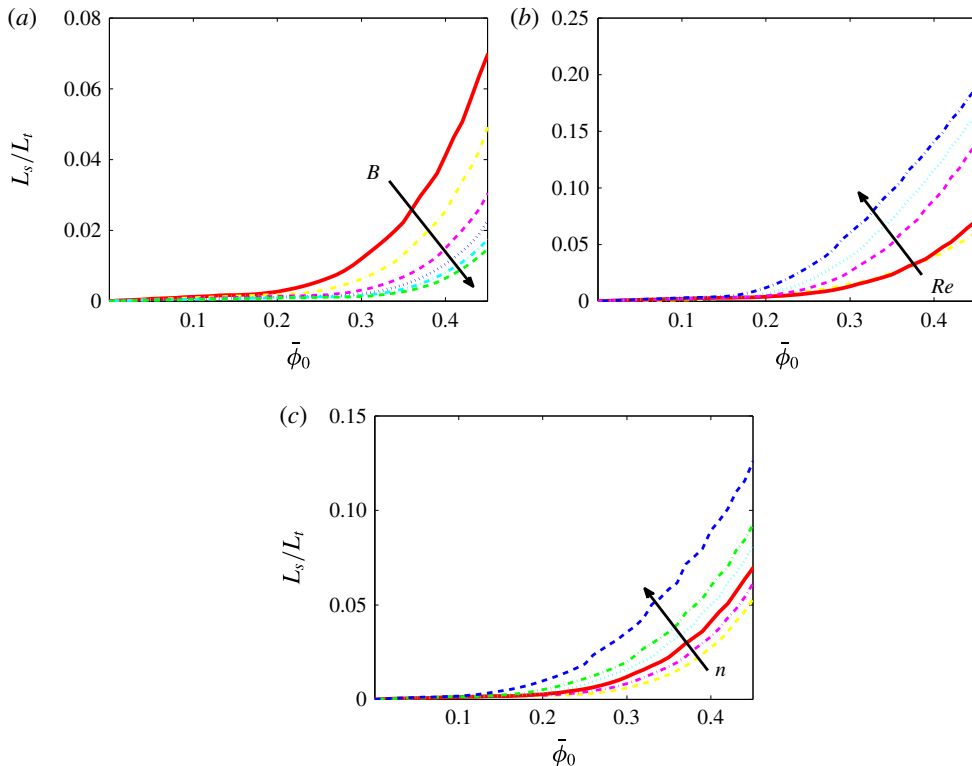


FIGURE 6. (Colour online) Scaled spreading length for a range of flow parameters:  $B = 1, 2, 4, 6, 8, 10$ ,  $Re = 1, 10, 100, 200, 400$  and  $n = 0.3, 0.4, 0.5, 0.6, 0.7, 1.0$ . The solid red line corresponds to the following representative set of dimensionless parameters:  $Re = 10$ ,  $B = 1$ ,  $n = 0.5$ ,  $Fr = 1$ ,  $s = 2.65$ ,  $\delta_p = 0.05$  and  $\delta_t = 0.0001$ .

#### 4.2.2. Spreading of a sequence of pulsed slugs

As discussed earlier in § 1, recent fracturing techniques such as CFT involve cyclic pumping of proppant slugs interspersed with clear fracturing fluid, with the intention of leaving open channels of clear fluid between the proppant slugs at the end of the operation, to form a series of pillars (in three dimensions) as the fracture pressure is released. If the pillars disperse into one another, then no increase in hydraulic conductivity is achieved. If the pillars are too far apart, then the fracture may pinch closed between pillars. Therefore, it is essential to engineer the optimal distance between the pillars. Our simple model provides a tool for exploring these aspects of flow design.

Figure 7 shows a sequence of proppant slugs pumped with the parameters of figure 4, using a slug length of  $T = 0.1$  and a spacing of 0.1 between slugs. We show colour maps of the solid volume fraction and scaled settling velocities at different times along the fracture. The spacing between the slugs decreases due to streamwise dispersion of solids, but the slugs remain separated. We now decrease both the spacing and pulsing time by a factor of 5; see figure 8. Two features are evident here. First, the dispersion length is larger than the spacing between slugs, so that open channels are not achieved. Second, there exists a considerable depleted region outside the pseudo-plug with scaled settling velocity of more than 2.

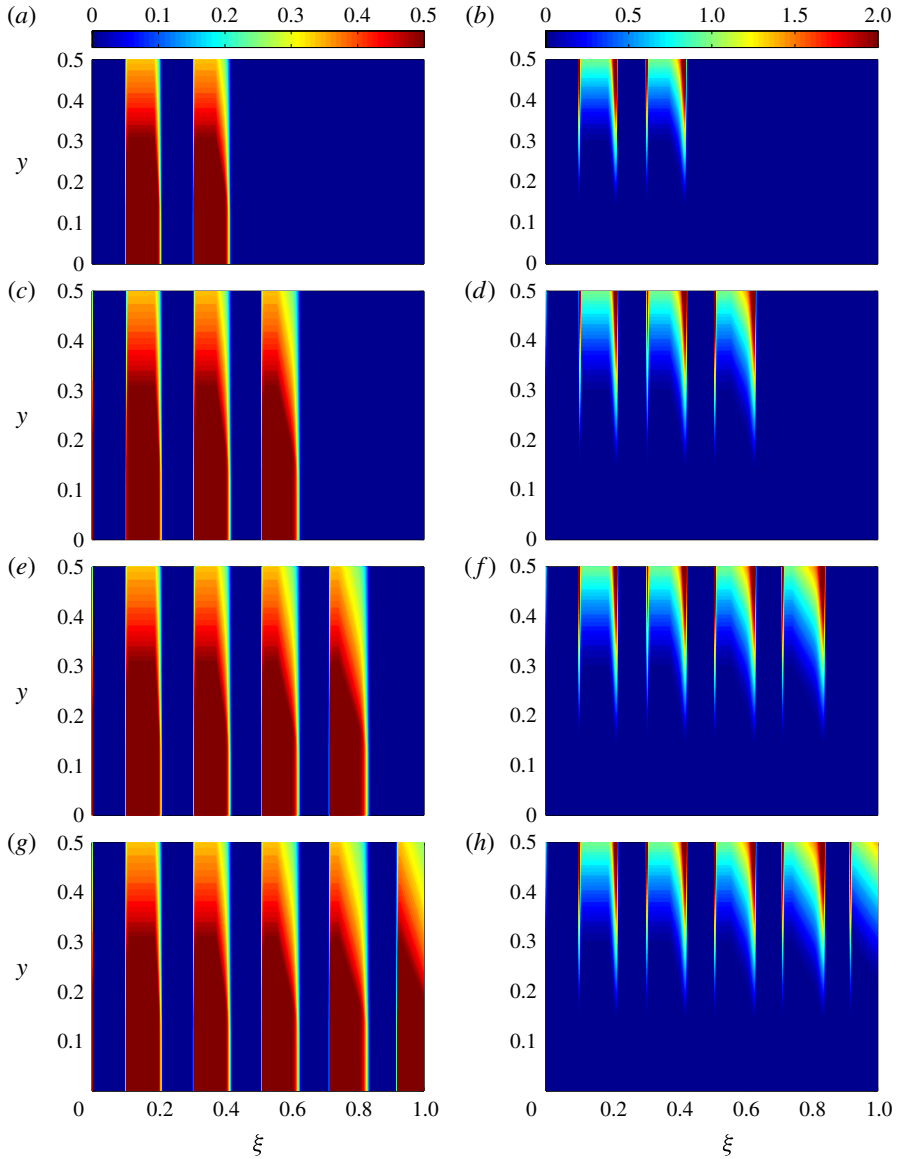


FIGURE 7. (Colour online) (a,c,e,g) Colour maps of  $\phi_0$  for multi-pulse propagation. The pulsing time is  $T = 0.1$ . (b,d,f,h) Colour maps of scaled sedimenting velocity as a single pulse propagates. The sedimenting velocity is scaled with the sedimenting velocity of  $\bar{\phi}_0 = 0.5$  at corresponding maximum shear rate. Flow parameters are as in figure 5.

To study the effects of yield stress, inertia and shear thinning, we perform similar computations as in figure 9 for the following base parameters:  $Re = 10$ ,  $B = 1$ ,  $n = 0.5$ ,  $Fr = 1$ ,  $s = 2.65$ ,  $\delta_p = 0.05$  and  $\delta_t = 0.0001$ . The results at final time are given in figure 9. Figure 9(a,b) indicates the base set of parameters. In (c,d) we have changed the following parameters:  $n = 1$  and  $Fr = 1.6$ . Figure 9(e,f) increases  $Re = 400$  and  $Fr = 2.5$ ; and (g,h) increases  $B = 10$ . We see that for larger values of power-law index and Reynolds number compared to those of the base solution, the dispersion and the



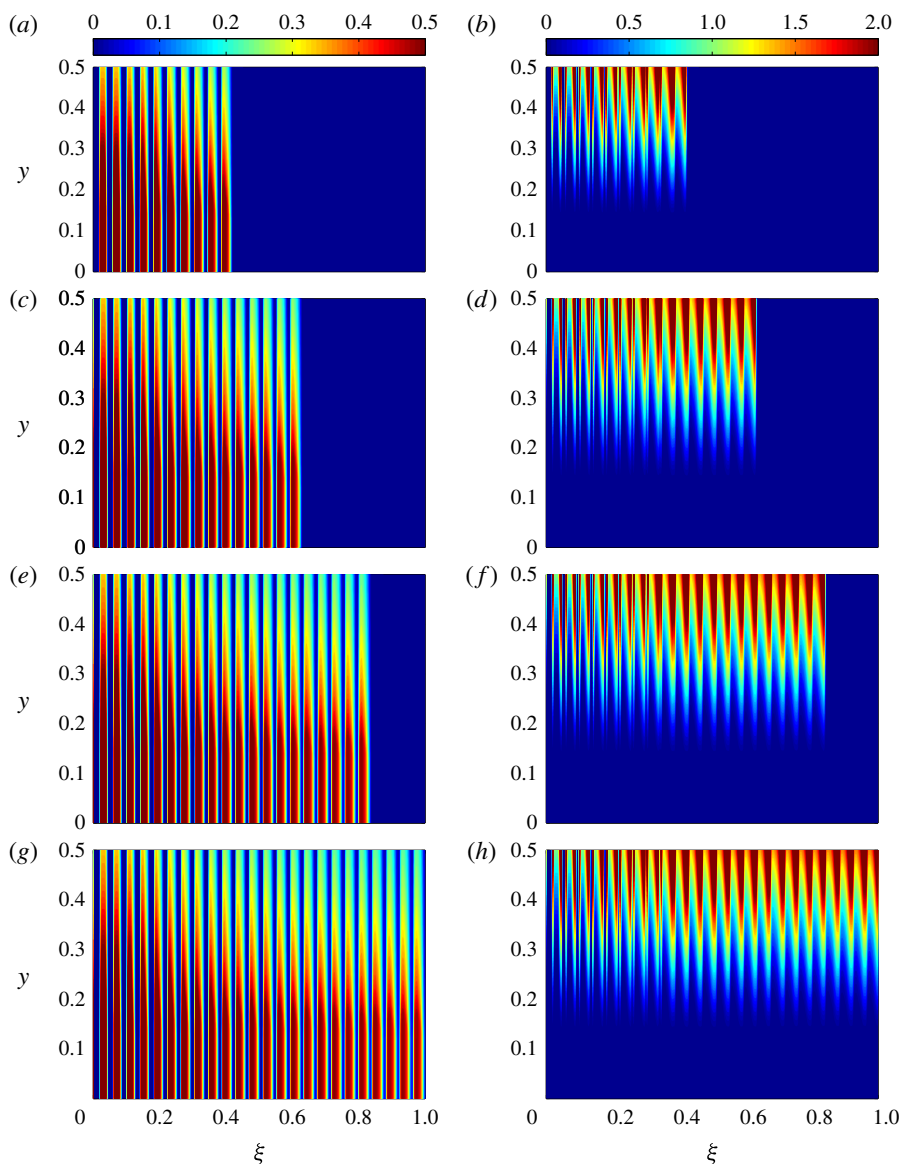


FIGURE 8. (Colour online) (a,c,e,g) Colour maps of  $\phi_0$  for multi-pulse propagation. The pulsing time is  $T=0.02$ . (b,d,f,h) Colour maps of scaled sedimenting velocity as a single pulse propagates. The sedimenting velocity is scaled with the sedimenting velocity of  $\phi_0=0.5$  at corresponding maximum shear rate. Flow parameters are as in figure 5.

depleted region near the wall are significantly larger. This suggests the possibility of slug interaction even with large time spacing between the pulses. We also see that, for a sufficiently large value of the yield stress, the dispersion is significantly reduced. This allows for control of slug interaction even with smaller time spacing and shorter slugs. Note also that the solids-depleted wall regions are significantly smaller.

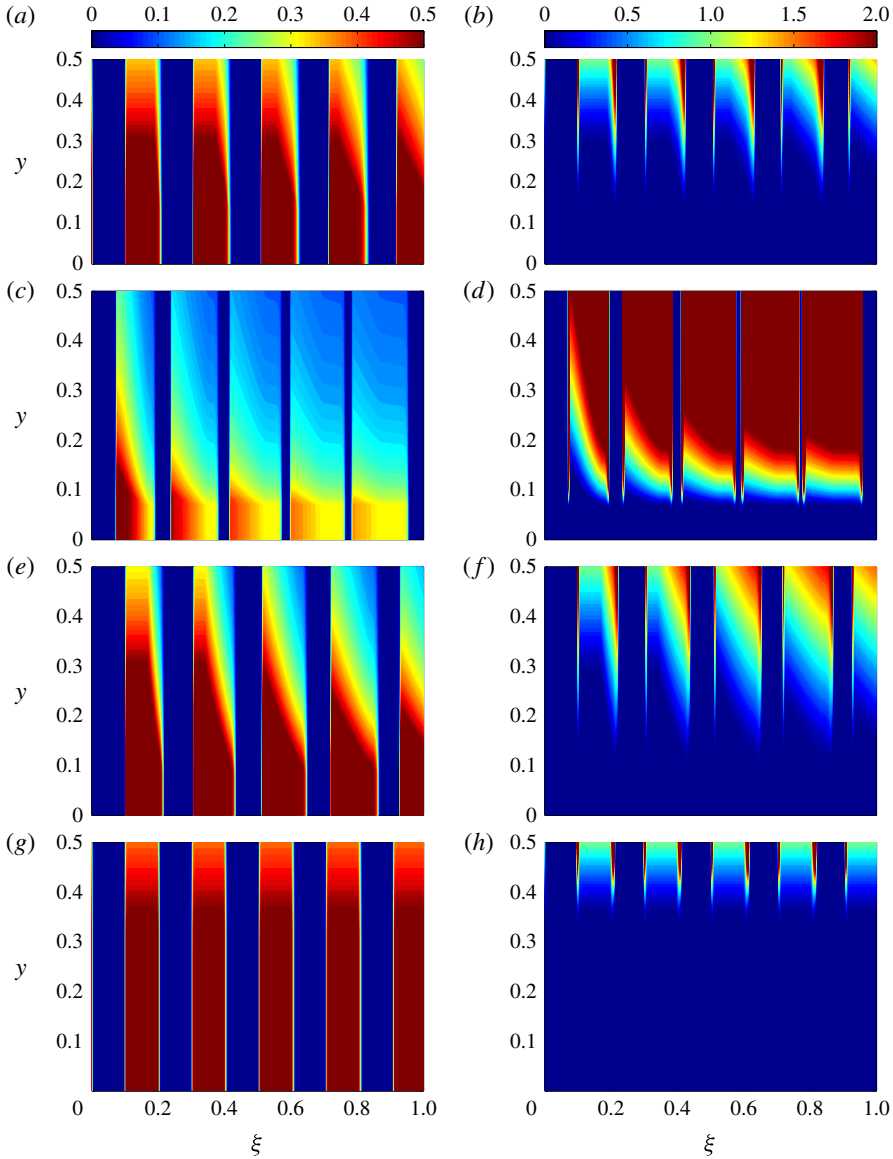


FIGURE 9. (Colour online) (a,c,e,g) Colour maps of  $\phi_0$  for multi-pulse propagation at  $T = 1$ . (b,d,f,h) Colour maps of scaled sedimenting velocity. The sedimenting velocity is scaled with the sedimenting velocity of  $\bar{\phi}_0 = 0.5$  at corresponding maximum shear rate. (a,b) Flow parameters as in figure 5. (c,d) Flow parameters as in figure 5 except  $n = 1$  and  $Fr = 1.6$ . (e,f) Flow parameters as in figure 5 except  $Re = 400$  and  $Fr = 2.5$ . (g,h) Flow parameters as in figure 5 except  $B = 10$ .

## 5. Discussion

We have developed a model that is suitable for investigating dispersion of solid particles within a yield stress fracturing fluid. This is targeted at various common fracturing scenarios, e.g. initial pad propagation, tip screen-out, as well as at newer techniques such as the channel fracturing technique (CFT). In each of these scenarios

a front between slurry and pure frac fluid exists and it is operationally important to predict the behaviour of this region.

We started with a comprehensive analysis of the range of hydraulic fracturing flows found. This revealed that typically a significant variation in the local particle Reynolds (and Stokes) number exists across the fracture due to the change in local effective viscosity of yield stress fracturing fluid. This is due to both the shear-thinning nature of the fluids and the presence of particles. In the central region (pseudo-plug region with high viscosity), Stokesian particle regimes are found. However, on entering the sheared regions and approaching the walls, large shear rates arise and the local particle flows become progressively inertial/unsteady. Hence, unlike Newtonian suspension, both Stokesian and inertial flow regimes may exist across the fracture.

The model framework developed is continuum-based and exploits the suspension balance methodology to model particle-phase transport and dispersion. The main novelties are that the SBM approach has been extended (i) towards yield stress fluids and (ii) to incorporate inertial/unsteady effects. The former uses recent rheological advances of Chateau *et al.* (2008) and Ovarlez *et al.* (2012, 2015). The latter uses scaling arguments stemming from Jenkins & McTigue (1990), Cassar *et al.* (2005), Boyer *et al.* (2011) and Andreotti *et al.* (2013), extended and found compatible with the recent results of Dagois-Bohy *et al.* (2015). Insofar as these aspects of the model are concerned, we acknowledge that significant work is still needed to fully calibrate the closures. What our work does is to provide motivation for the more focused studies that are needed to isolate flow effects and determine prefactors.

There exist model flow studies that may be adapted to yield stress fluid paradigms (e.g. Guazzelli & Morris 2012), and specialized rheometry techniques such as those of Dagois-Bohy *et al.* (2015) and Ovarlez *et al.* (2015) are evolving. Unlike Newtonian suspensions, computational techniques are significantly less evolved for yield stress fluids. In particular, loss of linearity prevents the application of methods such as Stokesian dynamics or others that resolve the particle dynamics economically via semi-analytical means. Instead, fully resolved computations appear the only tool and these are still painfully slow for yield stress fluid suspensions in three dimensions.

Later in this paper we have scaled and simplified the general model proposed. In the limit of thin and long fracture, an asymptotic method was used to derive a leading-order 1D model describing streamwise dispersion of solid volume fraction. The leading-order system of equations has been solved numerically for a range of fracturing flows. The results show a strong dependence of solid dispersion on both non-Newtonian rheology and inertial effects, as well as on process inputs. One main operational conclusion is that the use of a yield stress fluid may be exploited to limit the dispersion of proppant slugs transported within the fracture. Although the model itself is novel and the results are interesting from an industrial perspective, this remains a toy model. We are cautious about the industrial application, as this 1D model is mainly intended to be illustrative of what may be predicted by developing the broader framework in § 3.2.1 into two dimensions.

In further developing a 2D model following § 3.2.1, it is important to include leak-off effects (neglected here), as these will modify local solids fractions, as well as geometric variations in width and fracture orientation. The results shown have illustrated significant patterns of solids depletion and pseudo-plug propagation. In oriented 2D fractures, the consequences of such evolution may become apparent in large-scale solids settling patterns. Also we note that in two dimensions pulsed proppant slugs correspond to propagating layers of higher suspension viscosity interspersed with lower-viscosity pure fluid layers. Each such pair has both a

high–low and low–high viscosity front, the latter of which is likely to be vulnerable to fingering-type instability, possibly providing a break-up mechanism to form proppant pillars in the fracture. The study of such phenomena, as well as the effects of near-wellbore inflow conditions, fracture geometry and leak-off, are the main goals for a 2D model of this type.

Although the approach of § 3.2.1 (1D or 2D) allows study of transverse distributions of the flow variables, it is important to note that this is via post-processing and these variations are not explicitly coupled back into the model. One important phenomenon is that of so-called ‘convection’, in which a region of dense suspension (e.g. the pseudo-plug) moves as a dense single-phase fluid, settling rapidly. In the 1D approach this is not possible, as we have replaced the buoyancy term  $Re\phi_0/Fr^2$  by  $Re\phi_0/Fr^2$ , in order to simplify the modified pressure gradient by making it independent of  $y$ . To include this effect fully would necessitate integration across the fracture (numerically), resulting in what is sometimes called a 2.5D (or 1.5D) model similar to that outlined in § 3.2.2. Avoiding this and keeping to the simpler models means that the results may be interpreted/used to assess the risk of phenomena such as convection and predict solids depletion, but remain with some limitations. Developing the model in § 3.2.2 is a longer-term prospect, with significant complexity in developing closure expressions for both bulk inertial flows in complex geometries and the leading-order particle forces neglected (lift and centrifugal effects).

Finally, we should note that it is crucial to perform experimental studies to validate and refine our proposed framework. However, the experiments are challenging due to several limitations present in the available experimental methods, such as particle tracking velocimetry (PTV), nuclear magnetic resonance (NMR) and magnetic resonance imaging (MRI), e.g. lack of optical access for model yield stress suspensions to perform PTV, and poor temporal resolutions in MRI and NMR techniques. Recently, we have introduced a new technique based on X-ray radiography with high temporal ( $O(0.1\text{ s})$ ) and spatial ( $O(10\text{ }\mu\text{m})$ ) resolutions to study the evolution of solid volume fractions in fast suspension flows regardless of optical access and nonlinearity of the suspending fluids (Gholami *et al.* 2017). Currently, we are making use of this technique to study fracturing flows of yield stress fluids experimentally.

### Acknowledgements

The authors thank Schlumberger Oilfield Services for grant funding that initiated this research project. We also thank Dr D. Eskin of Schlumberger for many interesting discussions. Parts of this research were supported by NSF (grant no. CBET-1554044-CAREER) and ACS PRF (grant no. 55661-DNI9) via the research awards (S.H.).

### Appendix A. Inertial extension of the SBM using kinetic theory

Here we outline the extension of the SBM using kinetic theory. We start with the fluctuation energy balance for the entire suspension:

$$\frac{D}{Dt}\hat{E} = \hat{\Sigma} : \hat{\gamma} + \langle \hat{F}'_b \cdot \hat{u}' \rangle - \hat{\Phi} - \hat{V} \cdot \hat{q}, \quad (\text{A } 1)$$

where the prime denotes the fluctuation from the averaged value and where  $\hat{\Phi}$  is the average rate of dissipation of mechanical energy into heat. Here  $\hat{E}$  denotes the total energy,

$$\hat{E} = 3\phi\hat{\rho}_s\hat{\Theta} + (1 - \phi)\hat{\rho}_f\langle \hat{u}' \cdot \hat{u}' \rangle_f, \quad (\text{A } 2)$$

where the  $\langle \cdot \rangle_f$  indicates the average over the fluid phase. In practice, on assuming a fully developed flow and averaging across the gap, the left-hand side of (A 1) will be neglected, so there is little difference in considering  $\hat{E}$  rather than  $\hat{\Theta}$ . This is analogous to the neglect of  $C(\phi)$  in the SBM analyses of (2.29). Following Eskin & Miller (2008), we neglect the fluid phase part of the dissipation functional, approximating

$$\hat{\Sigma} : \hat{\gamma} \approx \hat{\Sigma}_p : \hat{\gamma}, \tag{A 3}$$

and we adopt the models from Sangani *et al.* (1996) and Wylie *et al.* (2003) for collisional and viscous contributions to  $\hat{\Phi} = \hat{\Phi}_c + \hat{\Phi}_v$ , i.e.

$$\hat{\Phi}_c = \frac{24}{\sqrt{\pi}}(1 - e)\phi^2\chi(\phi)\frac{\hat{\rho}_s\hat{\Theta}^{3/2}}{\hat{d}_p}, \tag{A 4}$$

$$\hat{\Phi}_v = 54\phi\frac{\hat{\eta}_f}{\hat{d}_p^2}\hat{\Theta}[R_{diss,0}(\phi) + Re_{p,\Theta}K_W(\phi)], \tag{A 5}$$

where  $e$  is the coefficient of restitution for particle collisions, and  $R_{diss,0}$  and  $K_W$  are dimensionless coefficients:

$$R_{diss,0} = 1 + 3\sqrt{\frac{\phi}{2}} + \frac{135}{64}\phi \ln \phi + 11.26\phi(1 - 5.1\phi + 16.57\phi^2 - 21.77\phi^3) - \phi\chi(\phi) \ln \epsilon_m, \tag{A 6}$$

$$K_W(\phi) = \frac{0.096 + 0.142\phi^{0.212}}{(1 - \phi)^{4.454}}. \tag{A 7}$$

Here  $\epsilon_m$  represents a scaled separation distance between particles at which hydrodynamic lubrication breaks down, i.e. effectively a roughness scale of the particles.

The dissipation rate terms contribute to the term  $\alpha$  in (2.29), which depends also on  $\hat{\Theta}$  in the inertial extension. This may be expanded in terms of  $Re_{p,\Theta}$ :

$$\alpha(\phi, \hat{\Theta}) = \frac{k_\alpha\eta_p(\phi)}{\phi} + \frac{9\phi R_{diss,0}}{2} + Re_{p,\Theta} \left( \frac{9\phi K_W(\phi)}{2} + \frac{2s}{\sqrt{\pi}}(1 - e)\phi^2\chi(\phi) \right). \tag{A 8}$$

Note that for the Stokesian regime  $\alpha(\phi)$  is defined only loosely in Nott & Brady (1994), to satisfy physical limits on  $\hat{\Pi}$  and  $\hat{\Theta}$  as  $\phi \rightarrow 0$  and as  $\phi \rightarrow \phi_m$ , which is unaffected by the inclusion of inertial terms. For  $Re_{p,\Theta} \neq 0$  and  $\phi \neq 0$  the zeroth-order dissipation above is modified significantly from that in Nott & Brady (1994) (i.e. by the term with  $R_{diss,0}$ ). This modification will, however, mostly affect the Stokesian central plug region of a fracture flow, reducing  $\hat{\Theta}$  there by a numerical factor. For simplicity, we neglect the phase slip term  $\beta(\phi)$  in (2.29) at this stage. The relative velocity may be important in dispersion, but here we are considering the contribution of the relative velocity to the distribution of  $\hat{\Theta}$ .

We modify the heat flux  $\hat{q}$  in a similar way to  $\alpha$ , combining the expressions from Nott & Brady (1994) and those from Gidaspow (1994):

$$\hat{q} = -3\hat{\eta}_f \left[ \kappa_{\theta,0}(\phi) + Re_{p,\theta} \left( \frac{150\sqrt{\pi}s\phi}{384(1+e)\chi(\phi)} \left[ 1 + \frac{6(1+e)\phi\chi(\phi)}{5} \right]^2 + \frac{2s(1+e)\phi^2\chi(\phi)}{\sqrt{\pi}} \right) \right] \hat{v} \hat{\theta}. \tag{A 9}$$

The zeroth-order term is a Stokesian term, related to the particle-phase viscosity. The two first-order terms in the expression above come from the kinetic theory of dense gases, and are related to kinetic and collisional effects, respectively (see Eskin & Miller 2008).

Finally, we modify the closures for the particle stress, in terms of both the particle pressure and particle-phase viscosity. Again we use (2.25) but with

$$\hat{\Pi} = \frac{\hat{\eta}_f \hat{\Theta}^{1/2}}{\hat{d}_p} \left[ 2\sqrt{3}k_\phi \phi^{1/2} \eta_p(\phi) + Re_{p,\theta} \frac{s\phi[1 + 2\phi\chi(\phi)(1+e)]}{\sqrt{3}} \right], \tag{A 10}$$

$$\frac{\hat{\tau}_p}{\hat{\eta}_f} = \left[ \eta_p(\phi) + sRe_{p,\theta} \left( \frac{5\sqrt{\pi}}{48(1+e)\chi(\phi)} \left( 1 + \frac{4}{5}(1+e)\phi\chi(\phi) \right)^2 + \frac{4(1+e)\phi^2\chi(\phi)}{5\sqrt{\pi}} \right) \right] \hat{y}. \tag{A 11}$$

The Stokesian term in (A 10) is as defined for the SBM, with the power-law index of  $\eta_p(\phi)$  fixed to 1 in order to reproduce the expected pressure behaviour ( $\hat{\Pi} \sim \phi^2$ ) as  $\phi \rightarrow 0$ . The form of  $O(Re_{p,\theta})$  terms chosen comes from kinetic theory, as in Gidaspow (1994). The modification of the particle deviatoric stress is selected to extend into the inertial regime the balance between the particle stress dissipation term and the term involving  $\alpha(\phi, Re_{p,\theta})$  in (A 1).

### A.1. Comparison

Using the above closures for fracturing flows is admittedly questionable. First, these closures are not able to fully model the dense suspension regime, where the whole system is connected via short-range, long-range and multi-particle interactions. Second, the range of density ratios  $s$  encountered in hydraulic fracturing falls below the usual range for which these closures were derived. However, inclusion of these closures allows a comparison with the direct scaling method used earlier and also serves to illuminate gaps in present physical understanding.

We now compute the fraction of the fluctuation energy dissipated by viscous and inertial effects:

$$\dot{\Phi}_{us} / \sum \dot{\Phi}_i = 1/(1 + sRe_{p,\theta}), \quad \dot{\Phi}_{es} / \sum \dot{\Phi}_i = sRe_{p,\theta}/(1 + sRe_{p,\theta}). \tag{A 12a,b}$$

We may compare the relative fractions of viscous and inertial dissipation, between the modified kinetic theory approach and the direct scaling approach earlier. This is done at  $\phi = 0.45$  and for  $s = 2.65$ . The results are shown in figure 10. We see that, for small values of the Stokes number ( $Re_{p,\theta} \leq 1$ ), the fluctuation energy is mainly dissipated by viscous effects in both approaches. However, when  $Re_{p,\theta} > 1$ , it is mainly inertial effects that contribute to the dissipation of the fluctuation energy in

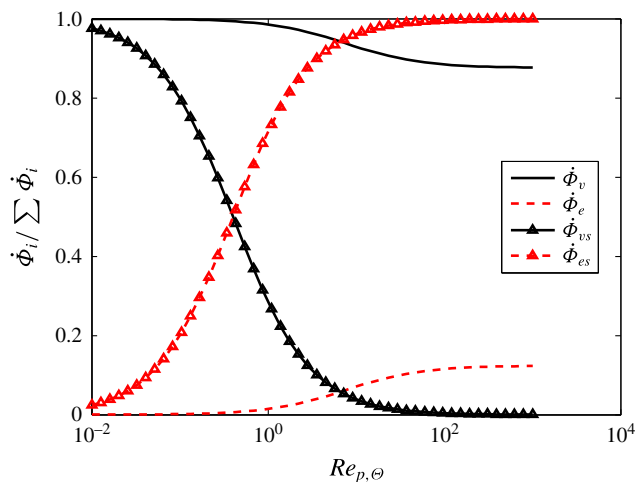


FIGURE 10. (Colour online) Comparison of the relative fractions of viscous and inertial dissipation for the modified kinetic theory approach and the scaling approach.

the direct scaling approach. In the kinetic theory approach, inertial effects dissipate only approximately 10% of the fluctuation energy. We see that kinetic approach does not appear to adequately capture the expected transition from viscous to inertial dominance. This motivates our adoption of the direct scaling approach. Of course, as commented already, the kinetic approach has been extended algebraically (and somewhat crudely) outside its domain of validity.

## Appendix B. Consequences of using the averaged buoyancy

Here we discuss the range of validity of approximating  $\phi(y)Re/Fr^2$  by  $\bar{\phi}Re/Fr^2$ , as we have done in order to make the zeroth-order problem tractable. The main question is whether the transversely varying buoyancy gradients become significant with respect to the gap-averaged gradients. In the first place, when considered as a regular perturbation procedure, we would expect that the leading-order approach is valid at least when  $Re\phi/Fr^2 \ll 1$ . We have seen that the system (4.5)–(4.10) leads to a unique leading-order solution. Let us now consider *a posteriori* the effect of replacing  $\bar{\phi}Re/Fr^2$  by  $\phi Re/Fr^2$  in the momentum balance. Assuming the pressure gradient is unchanged, then the relative error in the momentum balance is  $|\phi(y) - \bar{\phi}|Re/(Fr^2G)$ . When this quantity is relatively small, we might also expect that any correction in the pressure gradient terms that arises from using  $\phi(y)Re/Fr^2$  to have similar size, i.e. the argument is simply one of linearization. Of course, when this quantity becomes large, then the nonlinearity of (4.5)–(4.10) means that we can say very little.

Figure 11 plots  $|\phi(y) - \bar{\phi}|Re/(Fr^2G)$  for two representative values of  $Re/Fr^2$ , over a range of  $\bar{\phi}$  and for modest  $B$  and  $n$ . Comparing figures 11(a) and 11(b) reveals that, as expected, the errors are larger as  $Re/Fr^2$  grows. Perhaps surprisingly, for  $Re/Fr^2 \sim 10$  (figure 11a) the errors are small, and even for  $Re/Fr^2 \sim 60$  (figure 11b) the errors are less than 10% for dense suspensions ( $\bar{\phi} \geq 40\%$ ), which have been the focus of our study (see figures 5–10).

A number of factors contribute to keeping the errors smaller than might be expected. First, even in the case of a Newtonian fluid, with unit mean velocity through a channel

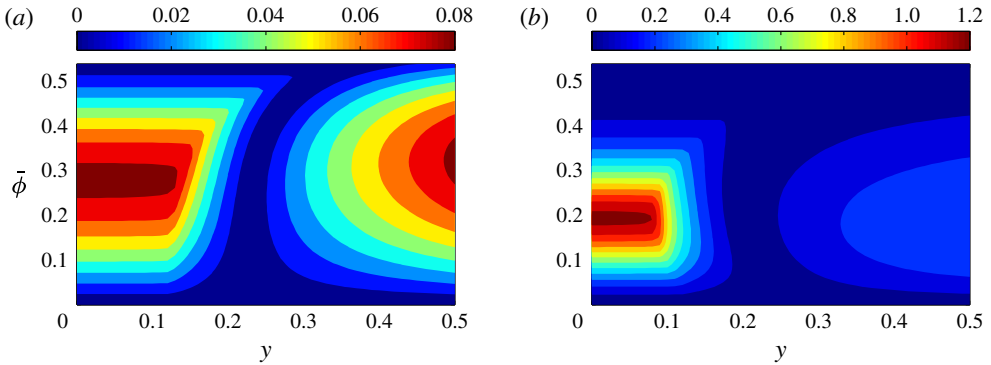


FIGURE 11. (Colour online) Colour maps of  $|\phi(y) - \bar{\phi}|Re/(Fr^2G)$  for a typical inertial fracturing flow with parameters (a)  $Re = 10$ ,  $B = 1$ ,  $n = 0.5$ ,  $Fr = 1$ ,  $s = 2.65$  and  $\delta_p = 0.05$  and (b)  $Re = 400$ ,  $B = 1$ ,  $n = 0.5$ ,  $Fr = 2.5$ ,  $s = 2.65$  and  $\delta_p = 0.05$ .

with unit width, the modified pressure gradient is  $G = 24$ . The pressure gradient is now increased by both rheology  $B$  and by the solids phase (although reduced by shear thinning). The point is that  $Re\phi/Fr^2 \ll 1$  is anyway conservative with respect to the typical pressure gradients encountered. Secondly, we note that the rheological effects combine to influence  $\phi(y)$  in a positive way, i.e.  $\phi(y)$  is more blunt than in a Newtonian suspension, which directly reduces the error  $|\phi(y) - \bar{\phi}|Re/(Fr^2G)$ . Two reasons for this are: (i) the velocity profiles and shear rates in shear thinning and yield stress fluids are more plug-like, which influences migration; (ii) as revealed in our model and as confirmed in Dagois-Bohy *et al.* (2015),  $\phi(y)$  approaches a critical value less than the jamming volume fraction at the channel centre. The latter means that  $\phi(y)$  must spread more. Note also that in figure 11 we have plotted results with a modest value of  $B$ . To conclude, our results suggest that the validity of our leading-order solutions extends beyond  $Re\phi/Fr^2 \ll 1$  to  $Re\phi/Fr^2 \sim 1$ , and even further depending on the specifics of  $\bar{\phi}$  and  $B$ . A more detailed study would be required to explore this and other limitations, e.g. particle depletion in wall layers. We note too that examining the errors in the leading-order model is further hampered since in our simplified approach, the two momentum equations in axial and vertical directions are replaced by a single momentum equation along the streamlines. This means that the information about the direction of the main flow is lost. A more comprehensive study of the model error is, however, planned for our future work.

Finally, one of the main issues in making the approximation of  $\phi Re/Fr^2$  by  $\bar{\phi} Re/Fr^2$  concerns what has been called ‘slurry convection’, whereby heavier and denser parts of the suspension may fall as a consolidated plug, balanced by an upflow of solids-depleted lighter fluid (closer to the walls). If such a situation occurs, the leading-order solution presented will not be valid (see also Dontsov & Peirce 2014). The point about slurry convection is that the local particle drag, which has relatively small relative velocity, is replaced by a bulk-scale buoyancy-driven motion, which allows for larger relative velocities. However, slurry convection is not well understood. The actual occurrence of slurry convection is not a simple matter of being able to develop a different 1D velocity solution following a different transverse description of the solids distribution. In particular, we should note that bulk exchange flows in pipes and channels frequently do not remain stratified with buoyancy balanced by viscous stresses. The rapid motions induced by buoyancy become balanced by bulk inertial



stresses, which leads to mixing, so that model-predicted 1D convection states are not always found in practice.

## REFERENCES

- AHNERT, T., MÜNCH, A. & WAGNER, B. 2014 Models for the two-phase flow of concentrated suspensions. Weierstrass Institute for Applied Analysis and Stochastics, *Preprint 2047* [http://www.wias-berlin.de/preprint/2047/wias\\_preprints\\_2047.pdf](http://www.wias-berlin.de/preprint/2047/wias_preprints_2047.pdf).
- ANDREOTTI, B., FORTERRE, Y. & POULIQUEN, O. 2013 *Granular Media: Between Fluid and Solid*. Cambridge University Press.
- ASMOLOV, E. S. 1999 The inertial lift on a spherical particle in a plane Poiseuille flow at large channel Reynolds number. *J. Fluid Mech.* **381**, 63–87.
- ASMOLOV, E. S., LEBEDEVA, N. A. & OSIPTSOV, A. A. 2009 Inertial migration of sedimenting particles in a suspension flow through a Hele-Shaw cell. *Fluid Dyn.* **44**, 405–418.
- ASMOLOV, E. S. & OSIPTSOV, A. A. 2009 The inertial lift on a spherical particle settling in a horizontal viscous flow through a vertical slot. *Phys. Fluids* **21**, 063301.
- AURADOU, H., BOSCHAN, A., CHERTCOFF, R., GABBANELLI, S., HULIN, J.-P. & IPPOLITO, I. 2008 Enhancement of velocity contrasts by shear thinning solutions flowing in a rough fracture. *J. Non-Newtonian Fluid Mech.* **153**, 53–61.
- AURADOU, H., DRAZER, G., BOSCHAN, A., HULIN, J.-P. & KOPLIK, J. 2006 Flow channeling in a single fracture induced by shear displacement. *Geotherm.* **35**, 576–588.
- AURADOU, H., DRAZER, G., HULIN, J.-P. & KOPLIK, J. 2005 Permeability anisotropy induced by the shear displacement of rough fracture walls. *Water Resour. Res.* **41**, W09423.
- BALHOFF, M. T. & THOMPSON, K. E. 2004 Modeling the steady flow of yield-stress fluids in packed beds. *AIChE J.* **50**, 3034–3048.
- BARBATI, A. C., DESROCHES, J., ROBISSON, A. & MCKINLEY, G. H. 2016 Complex fluids and hydraulic fracturing. *Annu. Rev. Chem. Biomol. Engng* **7**, 415–453.
- BATCHELOR, G. K. 1970 The stress system in a suspension of force-free particles. The stress system in a suspension of force-free particles. *J. Fluid Mech.* **41**, 545–570.
- BLEYER, J. & COUSSOT, P. 2014 Breakage of Non-Newtonian character in flow through a porous medium: evidence from numerical simulation. *Phys. Rev. E* **89**, 063018.
- BORONIN, S. A. & OSIPTSOV, A. A. 2014 Effects of particle migration on suspension flow in a hydraulic fracture. *Fluid Dyn.* **49**, 208.
- BORONIN, S. A., OSIPTSOV, A. A. & DESROCHES, J. 2015 Displacement of yield-stress fluids in a fracture. *Intl J. Multiphase Flow* **76**, 47–63.
- BOSCHAN, A., AURADOU, H., IPPOLITO, I., CHERTCOFF, R. & HULIN, J.-P. 2007 Miscible displacement fronts of shear thinning fluids inside rough fractures. *Water Resour. Res.* **43**, W03438.
- BOSCHAN, A., AURADOU, H., IPPOLITO, I., CHERTCOFF, R. & HULIN, J.-P. 2009 Experimental evidence of the anisotropy of tracer dispersion in rough fractures with sheared walls. *Water Resour. Res.* **45**, W03201.
- BOSCHAN, A., IPPOLITO, I., CHERTCOFF, R., AURADOU, H., TALON, L. & HULIN, J.-P. 2008 Geometrical and Taylor dispersion in a fracture with random obstacles: an experimental study with fluids of different rheologies. *Water Resour. Res.* **44**, W06420.
- BOYER, F., GUAZZELLI, E. & POULIQUEN, O. 2011 Unifying suspension and granular rheology. *Phys. Rev. Lett.* **107**, 188301.
- BRADY, J. F. 2015 Reviving the suspension balance model. In *Symposium on Multi-Phase Continuum Modelling of Particulate Flows*, University of Florida, Gainesville, Florida.
- BRADY, J. F. & MORRIS, J. F. 1997 Microstructure of strongly sheared suspensions and its impact on rheology and diffusion. *J. Fluid Mech.* **348**, 103–139.
- BROWN, S. R. 1987 Fluid flow through rock joints: the effect of surface roughness. *J. Geophys. Res.* **92**, 1337–1347.

- BUKA, A., KERTESZ, J. & VICSEK, T. 1986 Transitions of viscous fingering patterns in nematic liquid crystals. *Nature* **324**, 424–425.
- BUKA, A. & PALFFY-MUHORAY, P. 1987 Transitions of viscous fingering patterns in nematic liquid crystals. *Phys. Rev. A* **36**, 1527–1529.
- CASSAR, C., NICOLAS, M. & POULIQUEN, O. 2005 Submarine granular flows down inclined planes. *Phys. Fluids* **17**, 103301.
- CHAPMAN, B. 1990 Shear-induced migration phenomena in concentrated suspensions. PhD thesis, University of Notre Dame.
- CHATEAU, X., OVARLEZ, G. & LUU TRUNG, K. 2008 Homogenization approach to the behavior of suspensions of noncolloidal particles in yield stress fluids. *J. Rheol.* **52**, 489–506.
- COUSSOT, P., TOCQUER, L., LANOS, C. & OVARLEZ, G. 2009 Macroscopic versus local rheology of yield stress fluids. *J. Non-Newtonian Fluid Mech.* **158**, 85–90.
- DAGOIS-BOHY, S., HORMOZI, S., GUAZZELLI, E. & POULIQUEN, O. 2015 Rheology of dense suspensions of non-colloidal spheres in yield-stress fluids. *J. Fluid Mech.* **776**, R2.
- DBOUK, T., LOBRY, L. & LEMAIRE, E. 2013 Normal stresses in concentrated non-Brownian suspensions. *J. Fluid Mech.* **715**, 239–272.
- DONTSOV, E. V. & PEIRCE, A. P. 2014 Slurry flow, gravitational settling and a proppant transport model for hydraulic fractures. *J. Fluid Mech.* **760**, 567–590.
- DOUGHERTY, T. J. 1959 Some problems in the theory of colloids. PhD thesis, Case Institute of Technology.
- DRAZER, G. & KOPLIK, J. 2000 Permeability of self-affine rough fractures. *Phys. Rev. E* **62**, 8076–8085.
- DRAZER, G. & KOPLIK, J. 2002 Transport in rough self-affine fractures. *Phys. Rev. E* **66** (2), 026303.
- DREW, D. A. 1983 Mathematical modeling of two-phase flow. *Annu. Rev. Fluid Mech.* **15**, 261–291.
- ENTOV, V. M. 1967 On some two-dimensional problems of the theory of filtration with a limiting gradient. *Prikl. Mat. Mekh.* **31**, 820–833.
- ESKIN, D. & MILLER, M. J. 2008 A model of non-Newtonian slurry flow in a fracture. *Powder Technol.* **182**, 313–322.
- FANG, Z., MAMMOLI, A., BRADY, J. F., INGBER, MZ. S., MONDY, L. A. & GRAHAM, A. L. 2002 Flow-aligned tensor models for suspension flows. *Intl J. Multiphase Flow* **28**, 137–166.
- FIROUZANIA, M., METZGER, B., OVARLEZ, G. & HORMOZI, S. 2016 The hydrodynamic interaction of two small freely-moving particles in a Couette flow of a yield stress fluid. *69th Annual Meeting of the APS Division of Fluid Dynamics*, Vol. 61, No. 20.
- FRIGAARD, I. A. & RYAN, D. 2004 Flow of a visco-plastic fluid in a channel of slowly varying width. *J. Non-Newtonian Fluid Mech.* **123**, 67–83.
- FRIGAARD, I. A. & RYAN, D. 2016 The hydrodynamic interaction of two small freely-moving particles in a Couette flow of a yield stress fluid. *69th Annual Meeting of the APS Division of Fluid Dynamics*, Vol. 61, No. 20.
- GADALA-MARIA, F. & ACRIVOS, A. 1980 Shear-induced structure in a concentrated suspension of solid spheres. *J. Rheol.* **24**, 799–814.
- GHOLAMI, M., LENOIR, N., HAUTEMAYOU, D., OVARLEZ, G. & HORMOZI, S. 2017 Time-resolved 2D concentration maps in flowing suspensions using X-ray. *J. Rheol.* (submitted).
- GIDASPOW, D. 1994 *Multiphase Flow and Fluidization: Continuum and Kinetic Theory Descriptions*. Academic.
- GILLARD, M., MEDVEDEV, O., PENNA, A., MEDVEDEV, A., PENACORADA, F. & D'HUTEAU, E. 2010 A new approach to generating fracture conductivity. In *SPE Annual Technical Conference and Exhibition held in Florence, Italy, September*, SPE Paper 135034.
- GUAZZELLI, E. & MORRIS, J. F. 2012 *A Physical Introduction to Suspension Dynamics*, Cambridge Texts in Applied Mathematics. Cambridge University Press.
- HAMMOND, P. S. 1995 Settling and slumping in a Newtonian slurry, and implications for proppant placement during hydraulic fracturing of gas wells. *Chem. Engng Sci.* **50**, 3247–3260.
- HAMPTON, R. E., MAMMOLI, A. A., GRAHAM, A. L., TETLOW, N. & ALTOBELLI, S. A. 1997 Migration of particles undergoing pressure-driven flow in a circular conduit. *J. Rheol.* **41**, 621–640.

- HASEGAWA, E. & IZUCHI, H. 1983 On steady flow through a channel consisting of an uneven wall and a plane wall. Part 1. Case of no relative motion in two walls. *Bull. Japan Soc. Mech. Engng* **26**, 514–520.
- HOGG, A. J. 1994 The inertial migration of non-neutrally buoyant spherical particles in two-dimensional shear flows. *J. Fluid Mech.* **272**, 285–318.
- JENKINS, J. T. & MCTIGUE, D. F. 1990 Transport processes in concentrated suspensions: the role of particle fluctuations. In *Two Phase Flows and Waves* (ed. D. D. Joseph & D. G. Schaeffer), The IMA Volumes in Mathematics and Its Applications, vol. 26, pp. 70–79.
- KRIEGER, I. M. 1972 Rheology of monodisperse lattices. *Adv. Colloid Interface Sci.* **3**, 111–136.
- LAKHTYCHKIN, A., VINOGRADOV, O. & ESKIN, D. 2011 Modeling of placement of immiscible fluids of different rheology into a hydraulic fracture. *Ind. Engng Chem. Res.* **50**, 5774–5782.
- LASHGARI, I., PICANOVA, F., BREUGEMC, W. P. & BRANDT, L. 2014 Laminar, turbulent and inertial shear-thickening regimes in channel flow of neutrally buoyant particle suspensions. *Phys. Rev. Lett.* **113**, 254502.
- LASHGARI, I., PICANOVA, F., BREUGEMC, W. P. & BRANDT, L. 2016 Channel flow of rigid sphere suspensions: particle dynamics in the inertial regime. *Intl J. Multiphase Flow* **78**, 12–24.
- LEBEDEVA, N. A. & ASMOLOV, E. S. 2011 Migration of settling particles in a horizontal viscous flow through a vertical slot with porous walls. *Intl J. Multiphase Flow* **37**, 453–461.
- LECAMPION, B. & GARAGASH, D. I. 2014 Confined flow of suspensions modelled by a frictional rheology. *J. Fluid Mech.* **759**, 197–235.
- LEIGHTON, D. & ACRIVOS, A. 1987 The shear-induced migration of particles in concentrated suspensions. *J. Fluid Mech.* **181**, 415–439.
- LEMAIRE, E., LEVITZ, P., DACCORD, G. & VAN DAMME, H. 1991 From viscous fingering to viscoelastic fracturing in colloidal fluids. *Phys. Rev. Lett.* **67**, 2009–2012.
- LEVEQUE, R. J. 2002 *Finite Volume Methods for Hyperbolic Problems*, Cambridge Texts in Applied Mathematics. Cambridge University Press.
- LHULLIER, D. 2009 Migration of rigid particles in non-Brownian viscous suspensions. *Phys. Fluids* **21**, 023302.
- LINDNER, A., BONN, D., POIRE, E. C., AMAR, M. B. & MEUNIER, J. 2002 Viscous fingering patterns of silica suspensions in polymer solutions: effects of viscoelasticity and gravity. *J. Fluid Mech.* **469**, 237–256.
- LINDNER, A., COUSSOT, P. & BONN, D. 2000 Viscous fingering in a yield stress fluid. *Phys. Rev. Lett.* **85**, 314–317.
- LIU, Y., GADDE, P. B. & SHARMA, M. M. 2007 Proppant placement using reverse-hybrid fracs. *SPE Prod. Oper.* **22** (3), 348–356.
- LYON, M. K. & LEAL, L. G. 1998 An experimental study of the motion of concentrated suspensions in two-dimensional channel flow, Part 1. Monodisperse systems. *J. Fluid Mech.* **363**, 25–56.
- MAHAUT, F., CHATEAU, X., COUSSOT, P. & OVARLEZ, G. 2008 Yield stress and elastic modulus of suspensions of noncolloidal particles in yield stress fluids. *J. Rheol.* **52**, 287–313.
- MAKINO, K., KAWAGUCHI, M., AOYAMA, K. & KATO, T. 2002 Transition of viscous fingering patterns in polymer solutions. *Phys. Fluids* **7**, 455–457.
- MARON, S. H. & PIERCE, P. E. 1956 Application of Ree–Eyring generalized flow theory to suspensions of spherical particles. *J. Colloid Sci.* **11**, 80–95.
- MAXEY, M. R. & RILEY, J. J. Equation of motion for a small rigid sphere in a nonuniform flow. *Phys. Fluids* **26** (1983), 883. doi:10.1063/1.864230.
- MERHI, D., LEMAIRES, E., BOSSIS, G. & MOUKALLED, F. 2005 Particle migration in a concentrated suspension flowing between rotating parallel plates: investigation of diffusion flux coefficients. *J. Rheol.* **49**, 1429–1448.
- MOBBS, A. T. & HAMMOND, P. S. 2001 Computer simulations of proppant transport in a hydraulic fracture. In *SPE Production Facilities*, SPE Paper 69212, pp. 112–121.
- MORRIS, J. F. 2009 A review of microstructure in concentrated suspensions and its implications for rheology and bulk flow. *Rheol. Acta* **48**, 909–923.
- MORRIS, J. F. & BOULAY, F. 1999 Curvilinear flows of noncolloidal suspensions: the role of normal stresses. *J. Rheol.* **43**, 1213–1237.

- NESSYAHU, H. & TADMOR, E. 1990 Non-oscillatory central differencing for hyperbolic conservation laws. *J. Comput. Phys.* **87**, 408.
- NOTT, P. R. & BRADY, J. F. 1994 Pressure-driven flow of suspensions: simulation and theory. *J. Fluid Mech.* **275**, 157–199.
- NOTT, P. R., GUZZELLI, E. & POULIQUEN, O. 2011 The suspension balance model revisited. *Phys. Fluids* **23**, 043304.
- OH, S., SONG, Y., GARAGASH, D. I., LECAMPION, B. & DESROCHES, J. 2015 Pressure-driven suspension flow near jamming. *Phys. Rev. Lett.* **114**, 088301.
- OVARLEZ, G., BERTRAND, F., COUSSOT, P. & CHATEAU, X. 2012 Shear-induced sedimentation in yield stress fluids. *J. Non-Newtonian Fluid Mech.* **177–178**, 19–28.
- OVARLEZ, G., BERTRAND, F. & RODTS, S. 2006 Local determination of the constitutive law of a dense suspension of noncolloidal particles through MRI. *J. Rheol.* **50**, 259–292.
- OVARLEZ, G., MAHAUT, F., DEBOEUF, S., LENOIR, N., HORMOZI, S. & CHATEAU, X. 2015 Flows of suspensions of particles in yield stress fluids. *J. Rheol.* **59** (6), 1449–1486.
- PATIR, N. & CHENG, H. S. 1978 An average flow model for determining effects of three-dimensional roughness on partial hydrodynamic lubrication. *Trans. ASME J. Lubr. Technol.* **100**, 12–17.
- PEARSON, J. R. A. 1994 On suspension transport in a fracture: framework for a global model. *J. Non-Newtonian Fluid Mech.* **54**, 503–513.
- PHILLIPS, R., ARMSTRONG, R., BROWN, R. A., GRAHAM, A. & ABBOTT, J. R. 1992 A constitutive model for concentrated suspensions that accounts for shear-induced particle migration. *Phys. Fluids A* **4**, 30–40.
- PUTZ, A., FRIGAARD, I. A. & MARTINEZ, M. D. 2009 On the lubrication paradox and the use of regularisation methods for lubrication flows. *J. Non-Newtonian Fluid Mech.* **163**, 62–77.
- QUEMADA, D. 1982 *Stability of Thermodynamic Systems* (ed. J. Casas-Vazquez & J. Lebon), Lecture Notes in Physics, vol. 164, pp. 210–247. Springer.
- RAMACHANDRAN, A. 2013 A macro transport equation for the particle distribution in the flow of a concentrated non-colloidal suspension through a circular tube. *J. Fluid Mech.* **2013**, 219–252.
- ROUSTAEI, A., CHEVALIER, T., TALON, L. & FRIGAARD, I. A. 2016 Non-Darcy effects in fracture flows of a yield stress fluid. *J. Fluid Mech.* **805**, 222–261.
- ROUSTAEI, A. & FRIGAARD, I. A. 2013 The occurrence of fouling layers in the flow of a yield stress fluid along a wavy-walled channel. *J. Non-Newtonian Fluid Mech.* **198**, 109–124.
- ROUSTAEI, A. & FRIGAARD, I. A. 2015 Residual drilling mud during conditioning of uneven boreholes in primary cementing. Part 2: Steady laminar inertial flows. *J. Non-Newtonian Fluid Mech.* **226**, 1–15.
- ROUSTAEI, A., GOSSELIN, A. & FRIGAARD, I. A. 2015 Residual drilling mud during conditioning of uneven boreholes in primary cementing. Part 1: Rheology and geometry effects in non-inertial flows. *J. Non-Newtonian Fluid Mech.* **220**, 87–98.
- SANGANI, A. S., MO, G. B., TSAO, H. K. & KOCH, D. L. 1996 Simple shear flows of dense gas–solid suspensions at finite Stokes numbers. *J. Fluid Mech.* **313**, 309–341.
- SAVINS, J. G. 1969 Non-Newtonian flow through porous media. *Ind. Engng Chem.* **61**, 18–47.
- SEGRE, G. & SILBERBERG, A. 1961 Radial particle displacements in Poiseuille flow of suspensions. *Nature* **189**, 209–210.
- SHAHSAVARI, S. & MCKINLEY, G. 2016 Mobility and pore-scale fluid dynamics of rate-dependent yield-stress fluids flowing through fibrous porous media. *J. Non-Newtonian Fluid Mech.* **235**, 76–82.
- SKJETNE, E., HANSEN, A. & GUDMONDSON, J. S. 1999 High velocity flow in a rough fracture. *J. Fluid Mech.* **383**, 1–28.
- SNOOK, B., BUTLER, J. E. & GUZZELLI, E. 2016 Dynamics of shear-induced migration of spherical particles in oscillatory pipe flow. *J. Fluid Mech.* **786**, 128–153.
- SULTANOV, B. I. 1960 Filtration of visco-plastic fluids in a porous medium. *Isv. Akad. Nauk AzSSR, Ser. Fiz. Mat. Tekh. Nauk* **5**, 820–833.
- TABUTEAU, H., COUSSOT, P. & DE BRUYN, J. R. 2007 Drag force on a sphere in steady motion through a yield-stress fluid. *J. Rheol.* **51**, 125–137.
- TRULSSON, M., ANDREOTTI, B. & CLAUDIN, P. 2012 *Phys. Rev. Lett.* **109**, 118305.

- VU, T.-S., OVARLEZ, G. & CHATEAU, X. 2010 Macroscopic behavior of bidisperse suspensions of noncolloidal particles in yield stress fluids. *J. Rheol.* **54**, 815–833.
- WIERENGA, A. M. & PHILIPS, A. P. 1998 Low-shear viscosity of isotropic dispersions of (Brownian) rods and fibres; a review of theory and experiments. *Colloids Surf. A* **137**, 355–372.
- WYLIE, J. J., KOCH, D. L. & LADD, A. J. C. 2003 Rheology of suspensions with high particle inertia and moderate fluid inertia. *J. Fluid Mech.* **480**, 95–118.
- YEO, I. W., DE FREITAS, M. H. & ZIMMERMAN, R. W. 1998 Effect of shear displacement on the aperture and permeability of a rock fracture. *Intl J. Rock Mech. Min. Sci.* **35**, 1051–1070.
- ZIMMERMAN, R. W., KUMAR, S. & BODVARSSON, G. S. 1991 Lubrication theory analysis of the permeability of rough-walled fractures. *Intl J. Rock Mech. Min. Sci. Geomech. Abstr.* **28**, 335–341.